

The relation between stars and gas in distant galaxies

Jacky Cao

Level 4 Project, MPhys Physics

Supervisor: Dr. Mark Swinbank

Department of Physics, Durham University

Submitted: 12th April 2019

Optical and spectroscopic observations of galaxies provide a way to understand the internal dynamics of the stars and gas within it. Data for the Hubble Ultra Deep Field (HUDF) from the Hubble Space Telescope and the Multi-Unit Spectroscopic Explorer (MUSE) on the VLT provides a potential sample of more than 10,000 galaxies. This data-set was reduced by considering objects with redshifts $z > 0.3$ and with V-band magnitudes brighter than 25.0 mag. The ~ 30 remaining galaxies were extracted and then analysed by fitting for different regions of the galaxy spectra. The [OII] emission feature was separated and fitted with a Gaussian doublet to represent the gas dynamics. Applying a Penalized Pixel-Fitting method (pPXF) to the entire spectrum could quantify the stellar dynamics, however various issues were encountered in this initial research which prevented the successful operation of the fitting routine. Various tests were performed and a different spectral template library was applied in an attempt to remedy the problems. The next step in future work will be based around isolating the source of the issues and then further extending the routine to consider variations to the spectra.



Contents

1.	Introduction
1.1.	Classification of galaxies
1.2.	Dynamical studies of galaxies along the Hubble sequence
1.2.1.	Angular momentum and the evolution of galactic dynamics
1.2.2.	Faber–Jackson and Tully–Fisher relations
1.3.	Galaxy formation models
1.3.1.	Gravity
1.3.2.	Stellar formation
1.3.3.	Hydrodynamics
1.4.	The Hubble Ultra Deep Field
1.4.1.	HST
1.4.2.	MUSE
1.5.	Project study and aims
2.	Observations and data reduction
2.1.	HST XDF HUDF
2.1.1.	XDF data and data reduction
2.1.2.	Coloured HUDF
2.2.	MUSE HUDF
2.2.1.	MUSE data and data reduction
2.3.	Production of galaxy sample
3.	Discussion
3.1.	Galaxy velocity dispersions
3.1.1.	[OII] modelling
3.1.2.	Absorption line modelling
3.1.3.	σ comparisons
3.2.	Galaxy velocities
3.3.	Voronoi tessellation
3.3.1.	Tully–Fisher
3.3.2.	Faber–Jackson
3.4.	Limitations and future studies
4.	Conclusions
A.	Remaining galaxies from sample
B.	Voronoi Faber–Jackson plot

1. Introduction

1.1. Classification of galaxies

Edwin Hubble in 1926 was the first to classify galaxies into ellipticals, spirals, and irregulars (Hubble 1926). Reducing a sample of 400 extra-galactic objects through studying their morphological features, they were able to produce the *Hubble sequence* or *Hubble Tuning Fork*.

As demonstrated by Figure 1, ellipticals are codified by E_n , where n represents the integer galaxy ellipticity ($([a - b]/a)$). E_0 equates to non-elliptical galaxies and E_7 corresponds to galaxies with the largest ellipticities.

Moving along the fork, lenticulars (S_0) were introduced as these galaxies contain a central bulge and disc but contain no visible spiral features, therefore a fourth grouping was subsequently added (Sandage 1961, 1975, Sandage & Bedke 1994).

Spirals have ellipticities greater than E_7 and are categorised by their structural composition. The first feature to consider is whether they contain a horizontal bar which intersects the central galactic nucleus; if they do then they are barred spirals (SB), otherwise they are normal spirals (S). Both of these groups are split into three additional classes: “early” (Sa, SBa), “intermediate” (Sb, SBb), and “late” (Sc, SBC) types. Early spirals feature nebulosity centred in the nuclear region and closely coiled/unresolved arms, intermediates have large nuclear regions with thin arms, and late types have an inconspicuous nucleus and highly resolved arms.

If the structural features of a galactic object cannot be equated to those found in ellipticals, spirals, or lenticulars (e.g., a lack of a dominant nuclei and rotational symmetry), then they are sorted as irregular galaxies.

Subsequent identification schemes would refine and build on the Hubble sequence as larger datasets became more readily available. These would contain a greater variety of extra-galactic objects and allow for arguments such as expanding the spiral category due to the importance of rings and lenses

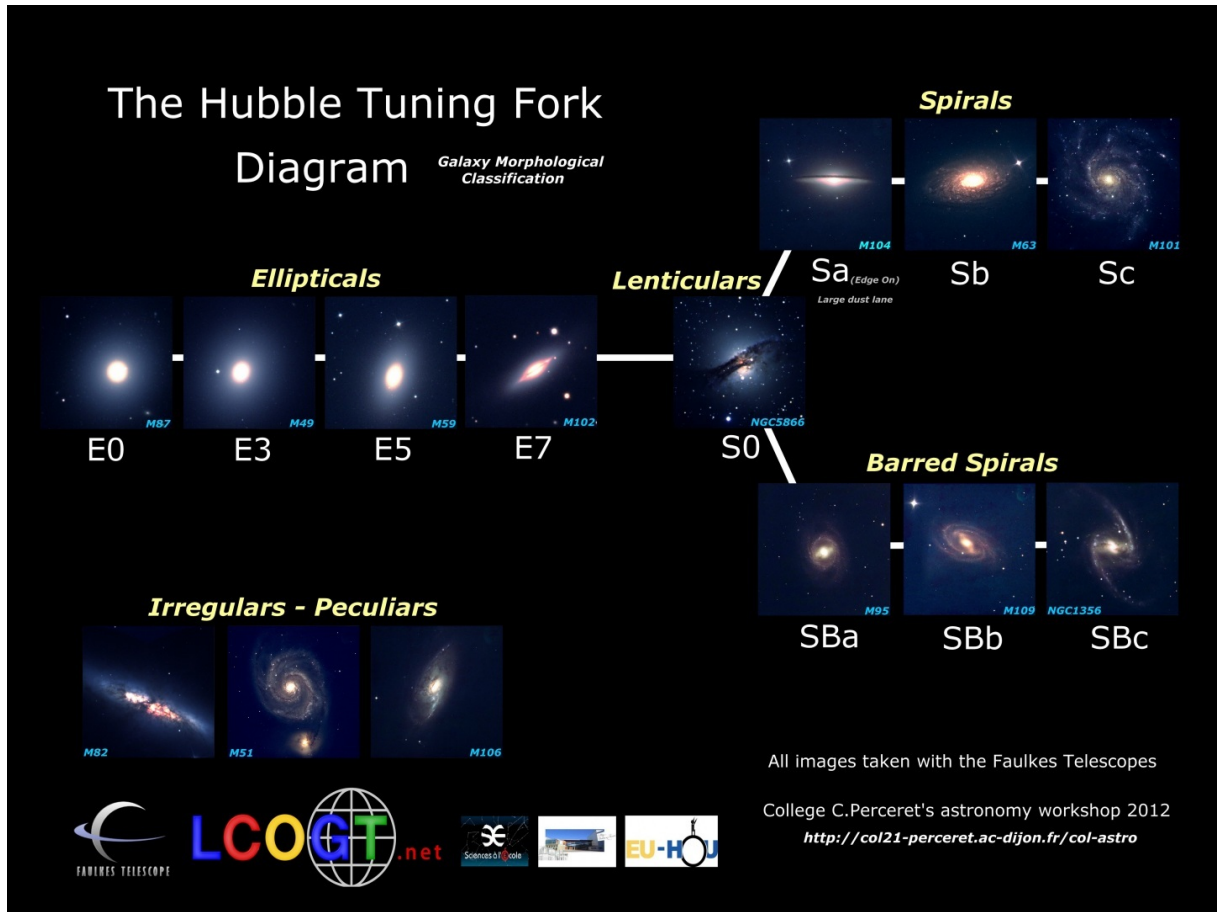


Figure 1. The Hubble sequence demonstrated graphically as the Hubble Tuning Fork (from Astronomie au collège PERCERET 2012). This diagram illustrates Hubble’s classification of galaxies by their morphologies into ellipticals, spirals, lenticulars, and irregulars.

as their defining features (de Vaucouleurs 1959).

Through Hubble’s work, galaxies are comprehensively classified by their morphologies, however these do not fully reflect the internal content of a galaxy. For an indicator of the inner dynamics, fundamental parameters should be employed in tandem with the morphological classification.

1.2. Dynamical studies of galaxies along the Hubble sequence

1.2.1. Angular momentum and the evolution of galactic dynamics

The mass, energy, and angular momentum are three physical values which are used as a quantitative classification of a galaxy.

The angular momentum is of particular interest as the defining morphologies of a galaxy is most likely a result of the

primeval mass–angular momentum distribution (Sandage et al. 1970). The acquisition of this angular momentum in a protogalactic system was proposed by Peebles (1969) to be a result of the tidal interactions with nearby protogalaxies. Within a young spiral system, these tidal torques induce galactic spin and lead to massive extended haloes if spiral discs have radii comparable to present day observations. By extension, the dynamics of these discs and their stellar populations are modelled to demonstrate that their observed sizes and rotation velocities are consistent with the conservation of early angular momentum (Dalcanton et al. 1997, Mo et al. 1998).

Measurements of galactic specific angular momentum allows for the derivation of empirical relations between the stellar component of the angular momentum j_* and

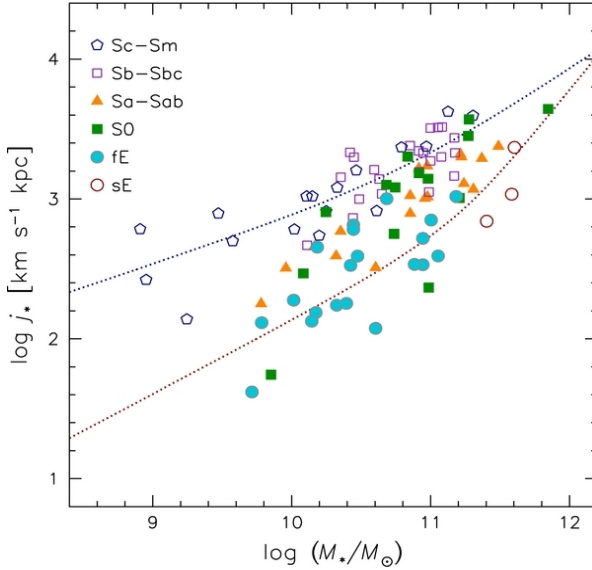


Figure 2. The total intrinsic specific angular momentum j_* against total stellar mass m_* for different galaxies (from Romanowsky & Fall 2012). Legend in upper left shows the galaxy types used. Ellipticals follow a similar relationship to spirals but with an offset of ~ 6 to lower j_* . This diagram represents one of the scaling relations for galaxies which reflect their internal dynamics.

mass M_* . These relationships can then be applied to describe the collective dynamics of galaxies (Fall 1983). If kinematic tracers are employed to measure j_* and M_* for large numbers of early-types (ellipticals and lenticulars) and late-types (spirals), then a plot such as Figure 2 reflects their dynamics by utilising independent variables and conserved physical quantities. The figure shows that both early and late types follow similar parallel trends which indicates an underlying connection between the physical parameters for galaxies.

This coupling between $j_* - m_*$ represents one of the *scaling relations* for galaxies. The importance of this particular relationship arises as it provides a fundamental scaling relation diagnostic for all galaxy types (Romanowsky & Fall 2012). With no full explanation available yet for the galaxy morphologies found in Hubble’s sequence, scaling relations provide an opportunity to understand the fundamental dy-

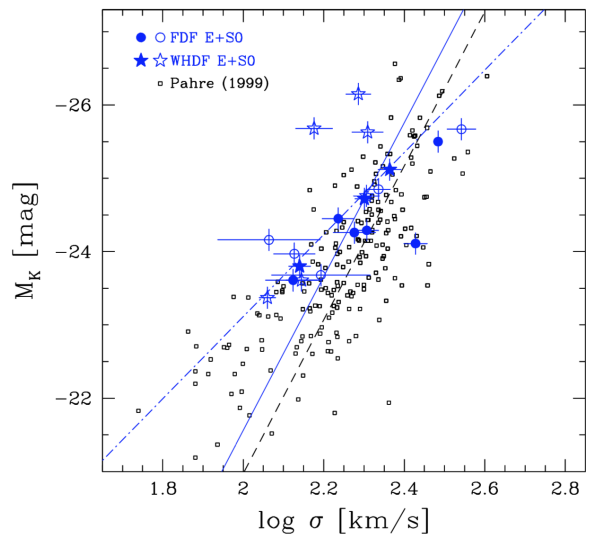


Figure 3. Faber–Jackson relation for early-type galaxies (from Fritz et al. 2009). Data contains elliptical galaxies from FORS Deep Field and the William Herschel Deep Field samples. The FJR relates the luminosity (M_K) with the velocity dispersion σ .

namics which may lead to a comprehensive model of galactic formation and evolution.

1.2.2. Faber–Jackson and Tully–Fisher relations

Despite the pairing between angular momentum and mass for various galaxy types (spirals, and ellipticals) as shown in Romanowsky & Fall (2012), scaling relations can be derived specifically for ellipticals and for spirals which would be better suited to describe their own specific properties within them.

For ellipticals, Faber & Jackson (1976) produced a scaling relation between galaxy luminosity and velocity dispersions. The latter variable was chosen because through the virial theorem, the mass of galaxies can be estimated. With the availability of larger datasets, plots such as Figure 3 illustrates the steady relationship between the luminosity and velocity dispersion. Through a well modelled Faber–Jackson relation, one potential use is to assess and understand galactic stellar populations and their evolutions (Fritz et al. 2009), an important component in galaxy modelling.

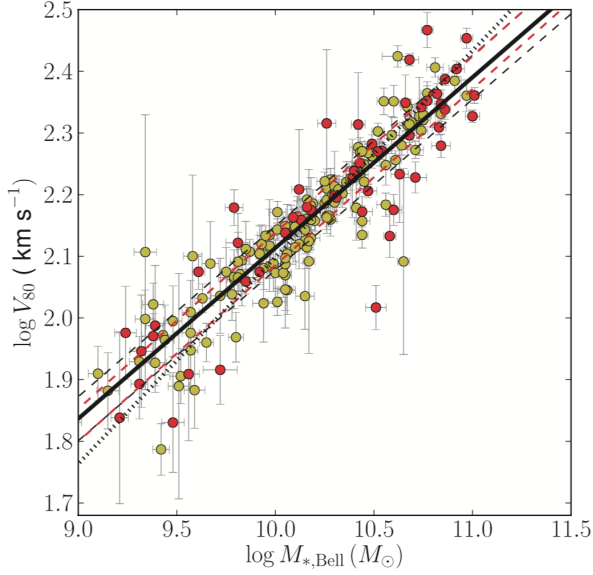


Figure 4. Tully–Fisher relation for spiral galaxies (from Romanowsky & Fall 2012). The TFR relates galaxy stellar mass M_* to the rotational velocity V .

On the other hand, Tully & Fisher (1977) derived a relation between the absolute magnitudes and H α emission line widths for spiral galaxies. Another form re-expresses this to couple the stellar mass and rotational velocity of a galaxy. Figure 4 demonstrates that there is a consistent relationship between these two parameters. In the production of this plot, Reyes et al. (2011) would calibrate several Tully–Fisher models to consider the contributions from galactic discs, stars, and dark matter. Through these calibrations, the Tully–Fisher relation, like the Faber–Jackson can be applied to the construction of galaxy formation and evolution models.

Both Faber–Jackson and Tully–Fisher relations (FJR and TFR) quantify the physical properties of observable galaxies. It would be natural to question whether they are applicable to galaxies at higher redshifts ($z > 0.3$) as these relations are calibrated with $z \sim 0$ galaxy samples. For local galaxies, their dynamics are measured using various tracers (stars, gas, and neutral hydrogen). Comparatively, galaxy dynamics at high redshifts can only be quantified from bright emission lines, which produces a sub-

jective view of galaxy dynamics. This partial bias is also found with the Hubble sequence where Hubble used local galactic objects as they provided the highest optical resolution to discern the different morphological features.

One potential method to demonstrate whether local scaling relations are applicable at high redshifts is through simulating galaxies at various stages of evolution with galaxy formation models.

1.3. Galaxy formation models

To produce a model which accurately describes the formation and evolution of galaxies, several physical processes must be accounted for. The main processes included in galaxy formation models are (Somerville & Davé 2015): gravity, star formation, hydrodynamics and thermal evolution, black hole formation and growth, star formation feedback, active galactic nucleus feedback, stellar populations and chemical evolution, and radiative transfer.

These processes interact and influence baryonic matter with the goal to create a dynamical galactic system. However, simulating these processes proves to be a challenge as there is difficulty in developing numerical algorithms which are able to accurately model their effects in a computationally efficient manner (Crain et al. 2015). Nonetheless, imperfect models are available for the component processes which simulate key observables and results.

By analysing gravity, stellar formation, and hydrodynamic processes, a condensed overview of galaxy formation can be produced. If these models are shown to be accurate then locally-calibrated scaling relations could be tested using models of high-redshift galaxies.

1.3.1. Gravity

For the underlying building blocks to be present for galaxy creation, gravity must be at hand to drive cosmic structure formation.

Employing cosmological models such as the Λ cold dark matter model (Λ CDM), early conditions in the Universe can be sim-

ulated to demonstrate how gravity can induce dark matter clustering (White & Rees 1978) and the condensation of dark matter halos (Navarro et al. 1996) to produce galaxies. Having an understanding of the distribution of dark matter halos in space is important in galaxy formation models as they reflect the overall distribution of mass.

As a result of the dark matter halos being dynamical objects, their gravitational interactions produce dynamical friction. This in turn can lead to the orbits of the galaxies within the halos to decay and eventually generate merger events. This transforms the structure and morphology of galaxies, and triggers additional star formation.

1.3.2. Stellar formation

With initial stellar formation in protogalaxies, the key concept to model is how gas evolves into stars. Observations show that dense, molecular clouds within the interstellar medium (ISM) collapse to become stellar birthing grounds. One of the ways to simulate the converging gas is through numerical modelling (Katz 1992), for example, assigning a Schmidt (1959) stellar formation rate (SFR) law to the gas. However, as with galactic formation modelling, the inclusion of additional physical processes (such as magnetic fields and turbulence effects) produces systems which are highly nonlinear and multidimensional (McKee & Ostriker 2007) thus more capable alternative methods are needed.

Madau et al. (1996, 1998) developed a physically motivated set of tools to reconstruct stellar formation. They employed integrated galaxy emission properties to trace the evolution of galaxy luminosity density as a function of redshift. As a quantified result, Figure 5 presents the ‘‘Madau plot’’ where SFRs are plotted against redshift for an epoch spanning from the present day to $z \approx 8$. Within their research they utilised galaxy observational data in the UV and IR to directly measure the SFR and subsequently constrained the initial mass function (IMF) of stars.

However, these methods do not provide

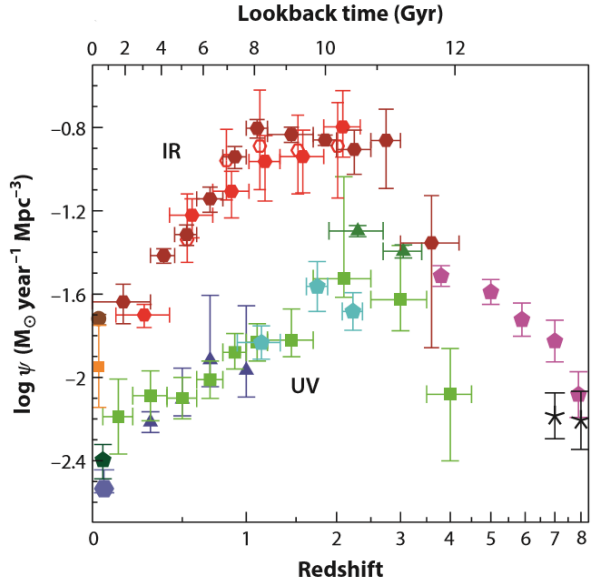


Figure 5. Stellar formation rate (SFR) densities against redshifts (from Madau & Dickinson 2014). The SFR history of the Universe is shown in the IR and UV for a period between the present day and $z \approx 8$.

the capability to model complex galaxy formation, instead, hydrodynamic simulations must be considered.

1.3.3. Hydrodynamics

Hydrodynamical modelling of galactic gas physics is the solving and evolution of hydrodynamic equations in a chosen gravity scheme. The *Evolution and Assembly of Galaxies and their Environments* (EAGLE) project implemented these equations to produce large scale N-body cosmological simulations (Schaye et al. 2015).

Using a Λ CDM universe, regions ranging in volume from 25 to 100 comoving Mpc were generated using numerical techniques and sub-grid models. They compared their EAGLE data with observations of the low-redshift universe to conclude that the simulation is generally able to replicate known observables. These include reproducing the galactic stellar mass function, disc galaxy sizes, and importantly producing agreement with the Tully–Fisher relation.

Figure 6 demonstrates that the EAGLE predictions are in remarkable agreement with the observational data. Cosmological

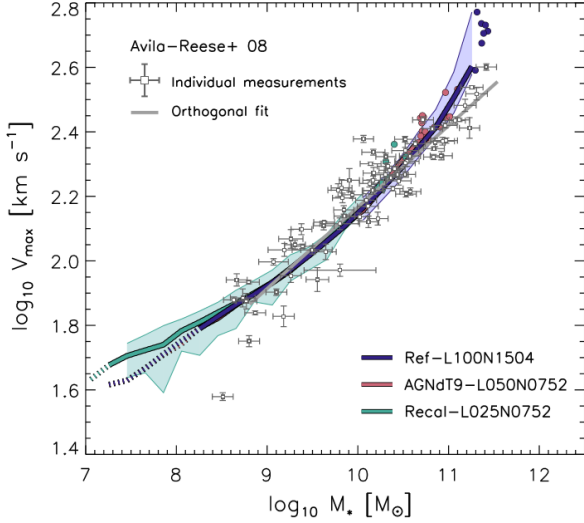


Figure 6. The Tully–Fisher relation (TFR) for spiral galaxies modelled with cosmological simulations (from Schaye et al. 2015). The TFR here is expressed as the relation between maximum rotation curve velocity V_{max} and stellar mass M_* . The legend in the lower right shows which simulated data was used, and the scatter points represent observational data.

simulations could therefore be an extremely useful tool in studying whether scaling relations evolve across cosmic history. These simulations have yet to be produced which offers a key opportunity to produce preliminary studies by utilising observational high-redshift galaxy data.

1.4. The Hubble Ultra Deep Field

In designing an experiment to test the applicability of scaling relations at high-redshifts, if data cannot be synthetically produced then it must be collected through observations.

1.4.1. HST

Optical data is the first out of two data-types required for a high-redshift analysis of scaling relations. One of the main constraints imposed on choosing a galaxy sample is the requirement for objects to be beyond redshift $z \approx 0$. The *Hubble Space Telescope* (*HST*) has produced such data in the form of deep observational surveys.

The Hubble Deep Field (HDF) was one

such survey. The expectation of HDF was to aid in resolving problems within studies of galaxy formation (Williams et al. 1996). Before HDF, observations of distant galaxies were limited by observational depth. The Canada-France Redshift Survey (Lilly et al. 1995) observed galaxies with redshifts $0.5 < z < 1.2$ in B and I -photometric bands. They determined that the central surface brightness of the disks in their spiral sample was more than 1.2 mag brighter than objects at $z \approx 0$, plus their B -band images appeared to be less regular than when observed at longer wavelengths. However, they did conclude that the observed galaxy morphologies at their redshift range were similar to those seen locally.

The HDF survey would utilise *HST*'s ability to resolve and image galaxy systems out to high redshifts. Data was collected for a four arcmin² field over an exposure period of 0.5 million s using Wide-Field Planetary Camera 2 (WFPC2) on *HST*. Four specific filters (F300W, F450W, F606W, and F814W) were chosen to try and balance image depth, colour information, and restrict the scattered light from Earth. The final reduced sample would contain 3000 galactic objects with a large number at $z > 1$. Driver et al. (1998) is one study which utilised the HDF sample to demonstrate that galaxy populations for high redshifts is markedly different than those at present times. For example, the $z > 2$ epoch appeared to contain a higher number of spiral and irregular galaxies which was attributed to the occurrence of more galaxy merger events.

To extend measurements to the period of recombination from $z \sim 6 - 10$ to $z \sim 1100$ required changes either in the observational method or with the observational instrument. The first observations of this epoch were made using the Sloan Digital Sky Survey through the detection of the Gunn-Peterson hydrogen edge in the spectra of distant quasars (Becker et al. 2001, Fan et al. 2002).

For an optical survey to observe large numbers galaxies at these redshifts, the lu-

minosity function inferred from the HDF suggested that data should be collected for a wider area but to a lesser depth than HDF. The Great Observatories Origins Deep Survey (GOODS; Giavalisco et al. 2004) performed such a survey with the optical component achieved by *HST*. Four filter bands (F435W, F606W, F775W, and F850L) were again used, but instead of WFPC2, the Advanced Camera for Surveys (ACS) was employed in it's place. From an observed area 30 times larger but 1 mag shallower than HDF, a sample of 60,000 galaxies was produced. Analysis of this data when coupled with K20 spectroscopic information would support the predominance of spirals and irregulars in $0.5 < z < 1.5$ galaxy samples (Cassata et al. 2005).

It was evident that with the success of deep surveys such as HDF and GOODS, naturally, an ultradeep survey would be commissioned to perform deeper galaxy formation studies, this was the Hubble Ultra Deep Field (HUDF). One of several goals for this project was to extend information on galaxies at the intermediate-redshift range $2 < z < 5$ and attempt to observe the reionisation boundary at $z \sim 6$ (Beckwith et al. 2006). The specifications of the data collection and data reduction for one version of the HUDF will be further discussed in Section 2.1.

An estimate of the number of galaxies at different redshifts was performed by assuming the galaxy luminosity distributions follow a Schechter function (Schechter 1976). Ranging from $1 < z < 7$ and with a magnitude limit between 28 and 29, a rough non-corrected value of 72700 sources was estimated to be observed in the HUDF. In reality, refined analysis and object detection algorithms such as SEXtractor (Bertin & Arnouts 1996) reduced this estimation to ~ 10000 objects, nonetheless, this is still an immense number of galaxies.

The data retrieved for the HUDF would later be combined with survey data from other *HST* projects (supernovae follow-up observations, HUDF09, CANDELS, and HUDF12) to produce the deepest image of

the sky ever taken in the optical/near-IR, the eXtreme Deep Field (XDF; Illingworth et al. 2013). Figure 7 contains a collapsed colour image for the HUDF region made using XDF data. The data from filters F775W, F606W, and F435W were combined into an RGB colour image. Representative of the same area, the XDF strived to enhance and augment the original HUDF data to provide a deeper dataset.

For studies of the early universe, the HUDF is a remarkable dataset. It provides high-resolution optical data for galaxies covering a wide range of redshifts which makes it highly suitable for studying changes in the characteristic luminosity, the evolution of morphologies, and the testing of locally-derived galaxy scaling relations.

1.4.2. MUSE

With optical data for high-redshift galaxies available in the form of the HUDF, testing scaling relations such as TFR and FJR additionally requires spectroscopic data to quantify redshifts, velocities and velocity dispersions.

It is generally known that calculating redshifts requires spectra of observed objects and for chemical elements or compounds, the value of which can be summarised as,

$$z = \frac{\Delta\lambda}{\lambda_{\text{emit}}} = \frac{\lambda_{\text{obs}} - \lambda_{\text{emit}}}{\lambda_{\text{emit}}}, \quad (1)$$

where z is the dimensionless quantity redshift, λ_{emit} is the emitted wavelength of an object, and λ_{obs} is the observed wavelength of an object (Zwicky 1933).

The application of redshifts to extragalactic astronomy has it's origins with Slipher (1913) who studied the radial velocities for the Andromeda galaxy. By attaching a spectrograph to a telescope, they were able to collect spectrograms for Andromeda and derive it's velocity with the Doppler approximation $z \approx v/c$. Slipher used the shifted spectral lines to calculate a mean velocity of -300 km s^{-1} and noted how this value for a spiral galaxy was much higher than the velocities stars. They had observed the

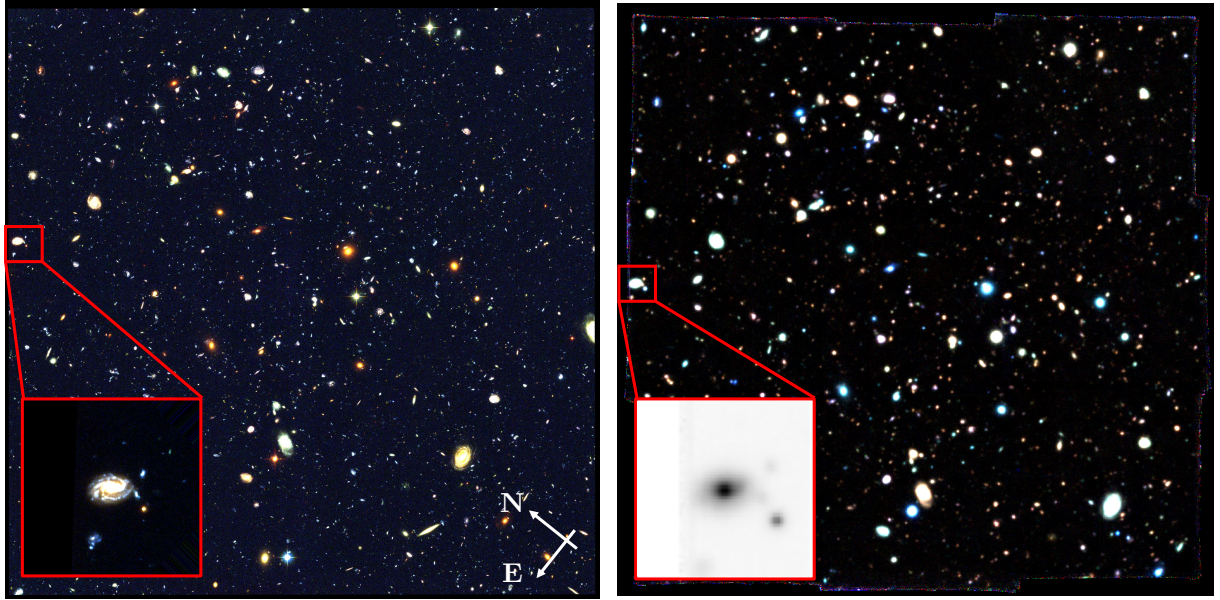


Figure 7. *Left-hand panel*: colour composite image at an image scale of 30 mas for the HUDF from *HST* ACS/WFC, Hubble eXtreme Deep Field project data (Illingworth et al. 2013). Frames in three filter bands (F775W, F606W, and F435W) were combined to represent the RGB channels within a colour image. *Right-hand panel*: colour image of the MUSE HUDF region. The spectra wavelength range (4650 Å–9300 Å) of the MUSE cube was divided into three equal regions (4650 Å–6180 Å, 6180 Å–7730 Å, 7730 Å–9300 Å), collapsed, and then combined to create an RGB image. Highlighted in both images is object RAF-24420 (Rafelski et al. 2015), the *HST* data has a higher optical resolution whereas the MUSE data outclasses in the resolution of the spectroscopic data.

effects of redshift on the spectra of galaxies, and arrived at the result that Andromeda is travelling towards us. Subsequent work (Slipher 1914) would also demonstrate the rotational motion of spiral galaxies. Through observing NGC 4594 with a spectrograph across the long axis of the galaxy, they obtained spectra with lines analogous to those produced by the diurnal rotation of a planet. Through the use of spectroscopy, Slipher was therefore able to establish the kinematic dynamics of galaxies.

Additional information can be obtained from galaxy spectra through measuring the widths of spectral lines. Also known as velocity dispersions, these widths encode a variety of knowledge related to the internal makeup of the galaxy. Measurements of the velocity dispersions for elliptical galaxies can be used to derive the galaxy masses with the virial theorem (Poveda 1958) and be used as an observational constraint on

galaxy formation theories (Fish 1964).

Alternatively, the velocity dispersions can be used to quantify the kinematics of stars and gas within the galaxies. The general method used: the stellar kinematics can be measured from the widths of the absorption lines in a galaxy spectra, and the gas kinematics properties from specific emission lines. Vega Beltrán et al. (2001) provides one example of this method for a sample of 20 nearby disc galaxies. They quantified stellar and gas velocities (V_* , V_g) and velocity dispersions (σ_* , σ_g) for integrated galaxy spectra to produce σ_g versus σ_* plots, and they then identified the dynamics across the galaxy's kinematic axis to produce rotation curves and velocity dispersion plots.

A spectra obtained for a galaxy therefore encodes vast amounts of information relating to its properties and dynamics. These derived values reflect and provide an insight into the formation and evolution of galaxies.

Type	Colour and notable lines
O	Hot blue-white (HeII, HeI)
B	Hot blue-white (HeI, HI)
A	White (Balmer, CaII)
F	Yellow-white (CaII, FeI, Cr,I)
G	Yellow (CaII, FeI, neutral metals)
K	Cool orange (CaII H and K, metals)
M	Cool red (TiO, VO, neutral metals)
L	Very cool, dark red, infrared (Molecular absorption, CrH, FeH, H ₂ O, CO, Na, K, Rb, Cs)
T	Coolest, infrared (CH ₄ , CO)

Table I. The Harvard Spectral Classification for stellar objects (Cannon & Pickering 1916). Stars are defined by their colour (temperature) and features seen from their spectra (Charity 2016, Payne 1925). Provided are spectral types, and their associated colour plus the main emission or absorption lines. Figure 8 provides examples of the possible observed spectra for spectral types OBAFGKM.

The star formation within a galaxy can be expressed with two particular functions (Miller & Scalo 1979): the spatially averaged rate of galaxy star formation (the stellar birthrate) and the frequency distribution of stellar masses at birth (the initial mass function, or IMF). The latter relationship is of particular interest as it allows for the derivation of the evolution, surface brightness, chemical enrichment, and baryonic content of galaxies (Chabrier 2003). Originally defined by Salpeter (1955), the IMF cannot be determined directly through observations, instead it can be indirectly constrained through methods such as using spectra absorption lines (van Dokkum & Conroy 2012).

Once obtained, the IMF provides an estimate of the present-day and initial stellar and brown dwarf populations of a galaxy. Knowledge of the IMF utilised with integrated galaxy spectra allows for the stellar

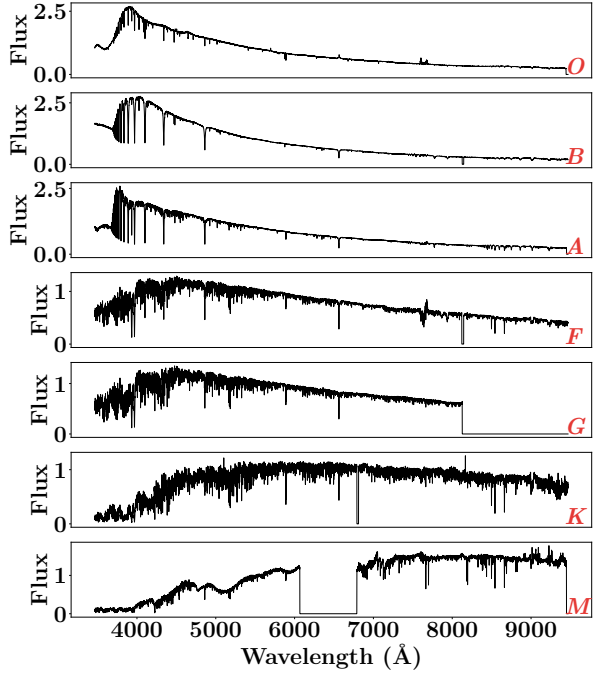


Figure 8. Example spectra for spectral types OBAFGKM. Taken from the Indo-US Library of Coud Feed Stellar Spectra (Valdes et al. 2004), the stars used have metallicities $[Fe/H]_{\odot} \approx 0$ and are: 30614 (O), 17081 (B), 39866 (A), 5015 (F), G 7-6 (G), 5858 (K), and G 176-11 (M). These spectra demonstrate that older types (FGKM) have larger amounts of absorption and emission lines when compared to younger types (OBA) as they have spent a greater amount of time undergoing nuclear fusion. Galaxy spectra will contain combinations of these stars which produces a unique profile.

types contained within the galaxy to be predicted.

An extrapolation can be performed as each star contains an individual spectral signature due to the elemental composition of the stellar atmospheres. Stars can be classified by absorption and emission lines and by optical colour to produce the Harvard Spectral Classification. Table I provides a summary of this classification scheme and Figure 8 contains examples of observed spectra for individual stellar types.

An alternative way to classify stars is through their metallicities. Denoted as Z or $[Fe/H]$, the metallicity is the measure of a star's chemical abundance and can be

found as the ratio between iron-to-hydrogen with respect to the Sun (Audouze & Tinsley 1976). The Sun is defined as $[\text{Fe}/\text{H}]_{\odot} \equiv 0$. Baade (1944) introduced stellar population groups which utilises metallicity: Population I are metal rich stars $[\text{Fe}/\text{H}] > -1$ found in discs, and Population II are metal poor stars $[\text{Fe}/\text{H}] < -1$ found in galaxy halos. A third group, Population III, has been theorised as stars which contain little to no metals $[\text{Fe}/\text{H}] < -3$ (Bond 1981). Spectroscopy can once again be utilised to calculate $[\text{Fe}/\text{H}]$ for Population I and II (Santos et al. 2004), Population III stars have yet to be observed but next-generation instruments such as ULTIMATE-Subaru provide the potential to do so (Moriya et al. 2019)

From the dynamics and kinematics of the stars and gas within the galaxy to calculating the stellar population, a wealth of information is obtainable from galaxy spectra. It is therefore unsurprising that spectroscopic data should be collected for high-redshift galaxies as there is no particular reason why the physics of the spectra would change. Coupled with optical data, the locally-derived scaling relations can then be tested and verified.

The Multi-Unit Spectroscopic Explorer (MUSE) on the Very Large Telescope (VLT) is one of the few current instruments which is able to provide spectroscopic data for redshifts $z > 6$ (Bacon et al. 2010). The key dataset obtained by MUSE which allows for the testing of the scaling relations is the MUSE Hubble Ultra Deep Field (Bacon et al. 2017). Specifics on the data collection and data reduction will be discussed in Section 2.2.

Though MUSE’s capability of integral field spectroscopy, deep spectroscopic observations were performed on the Hubble field to produce the MUSE HUDF which covers 90% of the original HUDF. Containing a wavelength range of 4650 Å to 9300 Å, the data for the MUSE HUDF can be collapsed into three regions (4650 Å–6180 Å, 6180 Å–7730 Å, 7730 Å–9300 Å) to produce an RGB colour image (Figure 7). When compared to the HST HUDF, the MUSE field

appears to have much lower optical resolution, however, this comparison is partly null as the primary use of the MUSE data is for spectroscopic analysis.

1.5. Project study and aims

With optical and spectroscopic data available for a large sample of high-redshift galaxies in the HUDF, this project seeks to understand whether locally-derived scaling relations are applicable to the high-redshift universe.

The paper is organised as follows. In Section 2 the observations and data reduction techniques will be described for the HST and MUSE HUDFs, and then the methodology provided for the construction of the galaxy sample used in this study. Section 3 presents the emission and absorption line modelling for the high-redshift galaxy spectra to obtain velocity dispersion and radial velocity values, the gas and stellar kinematics will be compared, the Voronoi tessellation work to test the Tully–Fisher and Faber–Jackson relations presented, the applicability of the scaling relations summarised and compared, and then a discussion of potential future studies. Finally, the conclusions will be presented in Section 4.

Cosmological quantities calculated in this study assumed a flat Universe with $H_0 = 70 \text{ km s}^{-1} \text{ Mpc}^{-1}$, $\Omega_m = 0.3$, and $\Omega_{\Lambda} = 0.7$.

2. Observations and data reduction

2.1. HST XDF HUDF

Optical images of galaxy morphologies were obtained from a colour composite HUDF frame created with publicly released XDF data¹.

2.1.1. XDF data and data reduction

Original imaging of the HUDF (Beckwith et al. 2006) employed the ACS Wide Field Camera (ACS/WFC) instrument on *HST* in four optical filter bands: F435W, F606W, F775W, and F850LP. The observations were obtained in 400 orbits between September 2003 and January 2004. Subsequent

¹ Available from: <http://xdf.ucolick.org>.

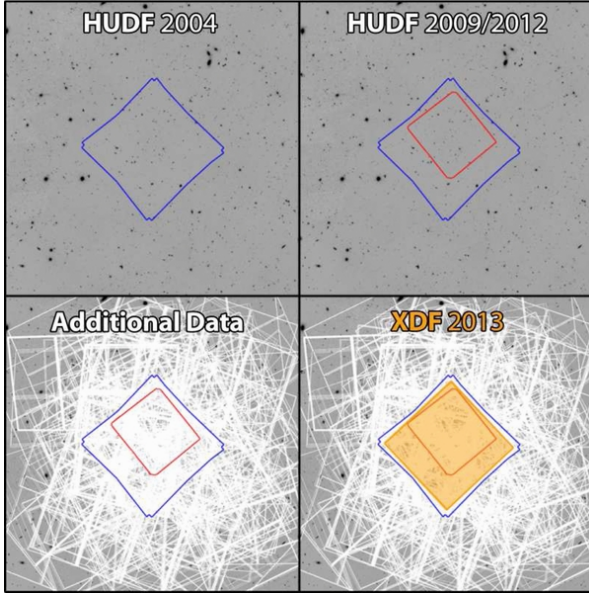


Figure 9. The production of the XDF (from Illingworth et al. (2013)). Upper left frame shows the original optical HUDF (blue) from ACS which contributed 50% of the XDF data set. Upper right shows the introduction of the HUDF09 IR data (red) from WFC3/IR, forming 20% of XDF. Lower left shows the final 20% contribution from 17 other *HST* programs (white) of which the large majority coming from CANDELS ACS and WFC3/IR data, and the HUDF12 WFC3/IR data. Lower right shows the final produced XDF frame (orange).

HST programs would re-image the region in optical and IR bands to further deepen the data available for the field. The XDF project combines all available data for the HUDF region from the period July 2002–December 2012 which were taken with ACS/WFC and *HST* Wide-Field Camera 3 Infra-Red (WFC3/IR) to produce the deepest ever field (Illingworth et al. 2013). Figure 9 shows the production of the XDF with the data from 20 *HST* programs.

For the ACS/WFC optical component, a field of 10.8 arcmin² was produced to a depth of 30.8(5 σ) AB mag in a 0.35'' aperture. 1972 exposures in five filter bands was utilised: 164 exposures for F435W, 286 exposures for F606W, 460 exposures for F775W, 362 exposures for F814W, and 700 exposures for F850LP. The XDF field

is centred on coordinates RA = 03^h32^m38.5^s and Dec. = -27°47'00.0" (J2000). The ACS/WFC channel includes two 4096 × 2048 pixel detectors at a scale of 0.05'' pixel⁻¹ to supply a 202'' × 202'' effective field of view.

As described by Illingworth et al. (2013), observations were chosen from the MAST *HST* archive for ACS/WFC by searching a 13 arcminute radius around the original HUDF coordinates ($\alpha = 03^{\text{h}}32^{\text{m}}39.0^{\text{s}}$, $\delta = -27^{\circ}47'29.0"$), and limiting the search to HST filters F435W, F606W, F775W, F814W, and F850LP, and exposure time to > 100 s.

The optical images in the XDF dataset were processed with the ACS calibration pipeline `calacs` (2012.2). This process subtracts bias, corrects for dark current, masks bad pixels, and performs flat-fielding. For images taken after *HST* Servicing Mission 4, they were corrected for charge transfer efficiency degradation (Anderson & Bedin 2010), bias shift, bias striping (Grogan et al. 2010), and amplifier crosstalk (Suchkov et al. 2010).

The data production pipeline applied to each filter dataset was `APSIS` (Blakeslee et al. 2003). Similar to the software package `MultiDrizzle` (Arribas et al. 2003), each image was passed through a drizzle–blot–drizzle cycle. Drizzling, or Variable-Pixel Linear Reconstruction, is a method where the resolution of undersampled images can be improved by using a shift-and-add technique and interlacing (Fruchter & Hook 2002). To blot is to map a median image onto the input plane of individual images, accounting for image shifts and geometric distortion.

Images would be background-subtracted and drizzled onto a tangential plane pixel grid. They would then be median-stacked and blotted back to each input image position and used as a template for cosmic-ray injection. A cosmic-ray mask would be generated for each image and combined with a data quality array. A final image mosaic would be produced by drizzling input images onto a single mosaic and combined with inverse-variance weight maps which

considers all noise sources (readout, dark current, and background noise).

The world coordinate system of each image was refined to produce precise registration across all ACS/WFC images because the pointing accuracy of *HST* is only good to within a few arcseconds. An image registration process was ran with `superalign` (Illingworth et al. 2013) where positions of a source were taken from a reference catalogue and from catalogues generated for each image, an accurate shift and rotation correction would then be calculated and applied to the input image. The reference catalogue was generated from combining the original HUDF F775W image with an astrometrically calibrated GOODS mosaic to provide accurate alignment for within and outside the HUDF area.

The final data produced would be a frame representing each filter band for ACS/WFC: F435W, F606W, F775W, F814W, and F850LP.

2.1.2. Coloured HUDF

To produce the colour image of the HUDF, the dataframes for F435W, F606W, and F775W were selected from the XDF dataset and combined into an RGB image using a Python routine. The filters correspond to the *I*-, *V*-, and *B*-bands, therefore they were used to approximately represent the B, G, and R channels within a colour image. The final coloured field can be seen in Figure 7.

2.2. MUSE HUDF

Primary analysis in this paper was performed on spectroscopic data for the HUDF from the MUSE HUDF Survey².

2.2.1. MUSE data and data reduction

Observations of the HUDF were performed with MUSE in Wide Field Mode on the VLT under the guarantee time observing ESO programs. Over the period September 2014–February 2016, 137 h of telescope time was used to cover the HUDF with a mosaic of nine MUSE fields (UDF-01 through UDF-09). Each MUSE field has

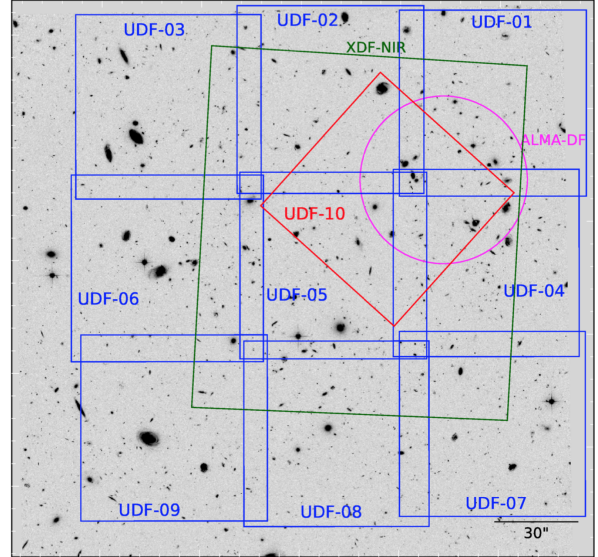


Figure 10. MUSE fields of the HUDF region (from Bacon et al. (2017)). The field location and orientation of the final `mosaic` (UDF01–09, blue) has been overlaid on the HST ACS F775W image. The UDF10 fields (red), XDF near-IR field (green), and ALMA deep field from the ASPECS pilot program (magenta, Walter et al. 2016) are additionally marked out.

the same area as the detector field of view, 1×1 arcmin 2 . The instrument has a spectral range of 4650–9300 Å, a spatial resolution of 0.2 arcsec, and a spectral resolution of $R \sim 3000$. Figure 10 presents the locations and orientations of the MUSE fields over the HUDF.

A total of 227 exposures were taken, each had an integration time of 25 minutes to limit the entry into the sky-noise-limited regime and to limit the impact of cosmic rays. The final `mosaic` of the HUDF achieved a depth of ≈ 10 h over an area of 9.92 arcmin 2 (90% of the original HUDF) within an approximate region of $3.15' \times 3.15'$.

An additional deeper observation was taken, UDF-10, over the deepest region of the XDF near-IR data and to overlap as much as possible with the deep ALMA pointing from the ASPECS pilot program (Walter et al. 2016). UDF-10 covers an area of 1.15 arcmin 2 and reaches a depth of 31 h.

As described by Bacon et al. (2017), the raw science data was reduced with

² Available from: <http://muse-vlt.eu/>.

the MUSE standard pipeline v1.7 dev. Individual exposures were processed by `scibasic` which employed daily calibrations (flatfields, bias, arc lamps, twilight exposures) and geometry table to produce a table containing all pixel information: location, wavelength, photon count, and an estimate of variance. Known bad pixels from CCD defects were masked. An illumination exposure was used to correct each exposure for flux variations at slice edges due to small temperature changes between morning calibrations and science exposures. The illumination exposures were chosen to be the ones nearest in temperature to the science frames.

The `scipost` pipeline would perform astrometric and flux calibrations on the table of pixel information. All flux calibration values obtained over all nights were scaled to the same mean level to remove transparency variations. The median of the stack was then obtained to produce the final reference response. A data cube would then be created with `makercube` using the default 3D drizzling interpolation process.

A self-calibration procedure was applied to correct for detector instabilities and imperfect flatfielding. A standard mask would be applied to all bright objects within the data. The median flux of each thin mirror slice of the MUSE image slicer was calculated for a bin of wavelength range 200–300 Å. The individual slices flux were offset to the mean of all slices and channels over same wavelength bin. Outliers would be rejected by using a 15σ clipping based on the median absolute deviation.

Inter-stack defects (dark or bright regions) at the edges of each slice stack for deep exposures of empty fields were additionally corrected for. An optimum mask was produced by median-combining all exposures onto an instrumental grid based on pixel coordinates, the locations of defects were identified to produce a bad pixel table. The 3D drizzle algorithm would introduce additional interpolation effects, so a 3D mask was produced for the cube by running the pipelines with and without the

bad pixel table.

Individual masks were produced and applied for specific defects such as Earth satellite trails or anomalous high dark levels or bias residuals.

The recentered and self-calibrated pixel table of each exposure would be sky subtracted with ZAP (Soto et al. 2016), and datacubes created on a fixed grid. A world coordinate system was pre-defined for the full mosaic region and frames UDF01–09 were projected onto the grid.

Variance and exposure properties for the datacubes would be subsequently calculated and derived as detailed by Bacon et al. (2017).

The 227 datacubes of the `mosaic` would be combined using estimated flux corrections from a reference *HST* image. A 5σ -clipping based on median absolute deviation estimates would be used to remove outliers, then an average performed on all volume sampling elements (voxels; $0.2'' \times 0.2'' \times 1.25 \text{ \AA}$). The corrected variance was propagated and an exposure map datacube produced. The final science datacube has a median depth of 9.6 h and contains $(n_x, n_y, n_z) = 947 \times 945 \times 3681 = 3.29 \times 10^9$ voxels. The cube has three axes: two tangential representing the field-of-view (arbitrarily defining them as x and y), and one extending perpendicular which contains the spectroscopic information (z).

In addition to the final data frame, a catalogue of 1574 objects was produced for both UDF10 and `mosaic` fields (Inami et al. 2017)³. This catalogue contains derived spectroscopic redshifts using the MUSE data, magnitudes found in several HST filters, and the flux values for various spectra emission peaks. The sources were extracted using a combination of the UVUDF catalogue (Rafelski et al. 2015) and directly from the MUSE cube with the methodology described in Bacon et al. (2017), Inami et al. (2017).

³ Available from VizieR with keyword J/A+A/608/A2: <http://vizier.u-strasbg.fr/viz-bin/VizieR>.

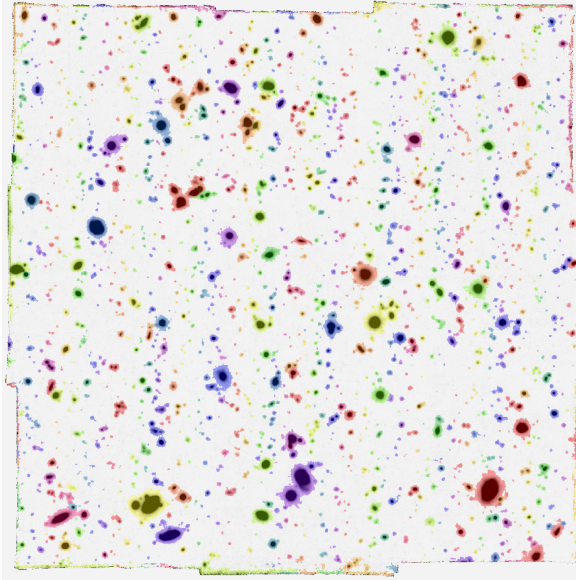


Figure 11. Galaxy segmentation map overlaid on collapsed 2D MUSE HUDF field. Segmentation map was created by **SExtractor** object extraction routine, each coloured area defines an individual object.

2.3. Production of galaxy sample

To produce the sample of galaxies used in this study, source extraction was performed on the MUSE datacube. The data was firstly collapsed into a single 2D frame by taking the median spectroscopic value along each voxel.

Source detection was then applied with the Starlink implementation (2018A; Currie et al. 2014) of the **SExtractor** package (Bertin & Arnouts 1996). Parameters were chosen to deblend galaxies, obtain their positions, and produce good signal-to-noise (S/N) values. The minimum number of connected pixels to register a detection was set to 5, no detection filter was specified, the zero-point in the photometry was set to 0.0, and the image scale set to match MUSE, 0.2 arcsec pixel $^{-1}$. A symmetric correction mask was chosen to account for overlapping objects, this mask replaced the overlap with counterparts symmetric to the objects centre. The FWHM seeing was set to 0.8 arcsec, and the size of the background mesh was set to 128.

Using these parameters, 1823 objects would be detected from the collapsed MUSE

frame. The exported catalogue from the extractor routine contains: object ID, x and y positions, the flux and associated error for the detected object, the RA and Dec., the semi-minor a and semi-major b axis values, the rotation of the object with respect to the horizontal, and a probability that the object is a star.

Alongside this catalogue a segmentation map was produced in tandem. Figure 11 shows this map superimposed onto the collapsed 2D MUSE field. Each galaxy during the extraction routine had a region and a unique ID defined for it, the segmentation map summarises this information into a single frame and allows for individual object masks to be produced to isolate the spectroscopic data for a specific galaxy. This would be particularly useful if two objects happened to overlap.

The **SExtractor** and MUSE catalogues were then combined so that the HST and redshift data would be accessible along with the extracted information. Employing Starlink’s TOPCAT software (Taylor 2005), the celestial coordinates in both catalogues were compared and matched using a sky algorithm within a maximum error of 1.0''. This would produce a combined catalogue to contain 837 objects.

For the purpose of the investigation into the applicability of local scaling relations, this sample was further reduced so only high S/N and high-redshift galaxies would remain.

The catalogue was first sorted by the MUSE spectroscopic redshifts and it was decided that 41 objects with $z < 0.3$ were to be removed, leaving 796 potential galaxies. This was defined because the project would use the bright [OII] $\lambda\lambda 3726,29$ Å emission doublet to quantify the dynamics of the gas and through considerations of the MUSE working spectral range beginning at 4650 Å, Equation 1 was employed with $\lambda_{\text{obs}} = 4800$ Å and $\lambda_{\text{emit}} = 3727$ Å to produce $z = 0.3$.

To enable analysis on a sample of just galaxies, the catalogue was organised by the **SExtractor** probability that the object is a star, and only objects with a probability less

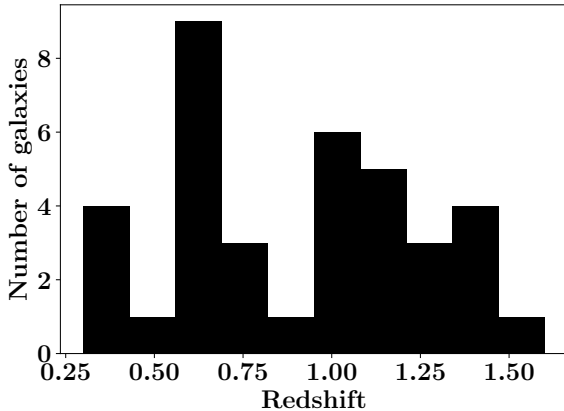


Figure 12. The redshift distribution of the final sample of 35 galaxies. There are a large number of galaxies focused at $z \sim 0.6$, but the majority are spread across higher redshifts $z \gtrsim 1.0$. With such redshift coverage, it is a good sample for the testing of scaling relations. Each bin represents a redshift width of 0.13.

than 0.50 were chosen. This would further reduce the sample to 252 potential galaxy objects.

Each of these sources were individually extracted from the MUSE mosaic cube. A 50×50 pixel² area was drawn around the central pixel coordinate of each object on the xy field-of-view plane, the matching spectroscopic data along z would be extracted, and the corresponding xy segmentation map area obtained.

With the 252 individual cubes, it had to be ensured that: the objects were in fact galaxies, an [OII] doublet feature could be found within the spectra, and enough S/N was present for the absorption lines to be modelled.

By organising the objects by their V-band magnitude and through [OII] doublet modelling (further discussion in Section 3.1.1), a magnitude limit of 25.0 mag was imposed on the sample. This was approximately the point where the fitting routine could recognise the [OII] doublet in the spectra and apply a model.

The remaining 75 sources were subsequently reduced to a final sample of 35 galaxies. The spectra for 40 of the ob-

jects were found to contain no particular [OII] feature which meant they could not be used for the later investigation. Table II and Table IV in Appendix A provides catalogue data and results from later analysis of galaxy spectra for the 35 objects. Figure 12 shows the distribution of the redshifts for the galaxies, a large number are at higher redshifts ($z \gtrsim 1.0$) which make them key for testing the locally-derived scaling relations.

Figure 13 demonstrates the sample reduction methods graphically where both plot the S/N versus V-band magnitude. However, the initial left-hand graph calculates the S/N from the flux and flux error provided by the MUSE catalogue, and the right-hand plot utilises the S/N calculated with the median and standard deviation of the region $(1+z) \times 3700 \text{ \AA}$ to $(1+z) \times 4500 \text{ \AA}$ in each galaxy spectra. This wavelength range was chosen as it was expected to contain the [OII] doublet and would be demonstrative of the signal.

With a sample of high-redshift galaxies obtained, it was now possible to begin isolating and modelling the spectra emission and absorption features to test whether locally-derived scaling relations are valid.

Note that within this paper, galaxies will be classified by their ID as defined by SExtractor (e.g., CXXXX), the corresponding Rafelski UVUDF ID is provided in Tables II, IV.

3. Discussion

3.1. Galaxy velocity dispersions

To quantify the gas and stellar kinematics of a galaxy, velocity dispersions were derived from modelling spectral features.

Before both of these analyses were performed, a single spectra representing each galaxy was required. This was found by masking the galaxy data with the segmentation map, collapsing all voxels into a galaxy-integrated spectra, and then logarithmically binning the data using a routine found in the package pPXF (Cappellari 2017).

Cube ID	RAF ID	RA (deg)	Dec. (deg)	F606W mag.	z	V_* (km s $^{-1}$)	σ_* (km s $^{-1}$)	V_{OII} (km s $^{-1}$)	σ_{OII} (km s $^{-1}$)
C1804	24420	53.1783773	-27.76824447	21.4864(8)	0.66850(6)	153531(10)	182(25)	153471(24)	147(35)
C1578	22735	53.13064889	-27.79026088	21.880(1)	0.66640(5)	153185(7)	117(12)	153094(18)	139(25)
C849	21651	53.17251203	-27.79636076	22.125(1)	0.347053(5)	89414(8)	3.8(7)	89314(18)	79(24)
C286	24587	53.16992265	-27.77102451	21.1412(9)	0.62169(1)	145050(7)	58(6)	144939(17)	91(16)
C5	20595	53.15639984	-27.81081513	21.5823(8)	0.66459(2)	152807(9)	78(10)	152768(21)	110(24)
C767	21364	53.18023505	-27.79892259	21.958(1)	0.6673(1)	153328(10)	148(21)	153250(24)	141(34)
C414	7253	53.15153909	-27.76201929	22.546(3)	0.42451(5)	106177(10)	106(21)	106076(23)	128(42)
C549	24515	53.15256871	-27.76950996	22.858(3)	0.33644(1)	87049(9)	25(6)	86943(22)	85(32)
C175	8246	53.18480046	-27.77745246	23.570(4)	0.52255(2)	126111(11)	127(25)	126029(28)	82(28)
C1129	9958	53.13928756	-27.78066897	23.677(4)	0.73403(2)	165114(19)	60(15)	165020(46)	95(41)
C765	23794	53.15817553	-27.78109416	22.391(2)	0.619373(2)	144615(12)	65(12)	144512(30)	64(20)
C1075	3630	53.16129898	-27.79547518	23.720(3)	0.30988(3)	80989(11)	143(41)	80925(26)	77(38)
C540	24348	53.16236468	-27.77506443	21.4602(8)	0.41894(2)	105015(8)	60(10)	104899(19)	91(25)
C895	39778	53.14168389	-27.77310068	24.291(6)	0.52461(2)	126561(18)	0.5(2)	126434(43)	73(38)
C554	38260	53.14916378	-27.76363345	23.401(3)	0.737184(4)	165687(12)	123(20)	165565(30)	70(19)
C109	9475	53.18591136	-27.77561507	24.084(4)	1.42553(8)	-	-	265631(137)	105(83)
C310	8531	53.16632928	-27.76858816	23.778(5)	1.29533(2)	-	-	249090(83)	75(39)
C363	8672	53.16395412	-27.76905273	24.569(7)	0.41891(3)	-	-	104894(57)	57(47)
C486	51705	53.18782913	-27.79405589	20.6113(5)	0.345393(8)	-	-	88944(12)	91(19)
C254	4686	53.19373778	-27.78787018	24.572(7)	0.43534(3)	-	-	108346(44)	48(30)
C759	8949	53.14617923	-27.77103939	24.108(5)	1.3155(2)	-	-	251719(134)	108(88)
C1394	2908	53.1525505	-27.80037599	24.99(1)	1.4254(1)	-	-	265614(101)	0.04(2)
C847	21703	53.17365111	-27.7973635	24.218(5)	0.66543(1)	-	-	152920(28)	34(10)
C1665	50714	53.15110943	-27.80949195	24.552(4)	1.08753(3)	-	-	220642(99)	79(54)
C541	24353	53.16081556	-27.77537746	22.442(2)	0.62149(6)	-	-	144902(21)	111(25)

Table II. Parameters for the final reduced sample of 35 galaxies. Columns show the working cube ID, the ID from the UVUDF Catalogs (Rafelski et al. 2015) (RAF ID), the object right ascension (RA) and declination (Dec.), the magnitude of the object in the HST F606W filter, the calculated galaxy redshift (z), the galaxy stellar velocity (V_*) and velocity dispersion (σ_*), and the galaxy gas velocity (V_{OII}) and velocity dispersion (σ_{OII}). Note that only 15 galaxies were analysed for their stellar and gas components as the majority of the sample contained spectra with not enough signal-to-noise. 11 of the non-analysed galaxies are provided here with the rest contained in Appendix A.

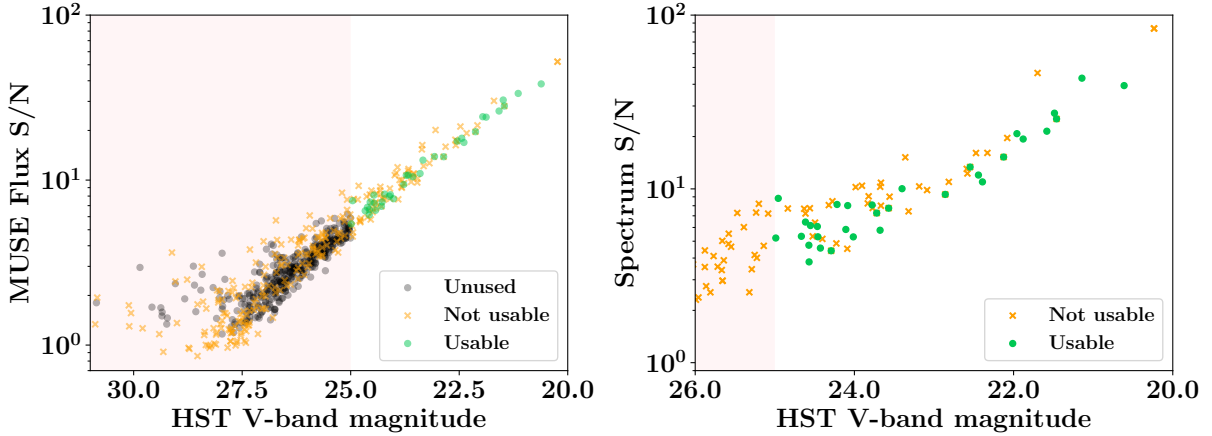


Figure 13. *Left-hand panel:* MUSE flux signal-to-noise (S/N) versus HST V-band magnitude for 252 extracted cubes. *Right-hand panel:* Spectrum S/N versus HST V-band magnitude for reduced sample of extracted objects. *Both:* final sample of 35 galaxies is indicated as “Usable” (green), and the red area indicates the imposed magnitude limit of 25.0 mag. The reduction of the cubes to produce the final sample was highly dependent on whether an object was a galaxy, if an [OII] feature was present, and whether there was enough S/N for visible absorption features. This gave rise to the “Not usable” (orange) classification as shown.

3.1.1. [OII] modelling

For the gas dynamics within these galaxies, the [OII] doublet was used as it is one of the brightest observable emission peaks at redshifts $0.3 \lesssim z \lesssim 1.6$. To define the final sample of galaxies, a routine was ran to find whether the doublet could be found within the region $(1+z) \times 3600 \text{ \AA}$ to $(1+z) \times 3750 \text{ \AA}$, and if the following Gaussian model could be fitted to the doublet,

$$f_{[\text{OII}]}(x) = cx + \frac{I_1}{\sigma\sqrt{2\pi}} \exp\left(-\frac{(x - L_1)^2}{2\sigma^2}\right) + \frac{I_2}{\sigma\sqrt{2\pi}} \exp\left(-\frac{(x - L_2)^2}{2\sigma^2}\right), \quad (2)$$

where x are the redshifted wavelengths, c is a constant, I_1 and I_2 are scaling factors limited by I_1/I_2 , L_1 and L_2 are the [OII] peaks (3727.092, 3729.875 Å) multiplied by $(1+z)$ with z as a free parameter, and σ is the quadrature sum of a constant instrumental resolution σ_{inst} and the deconvolved width of the doublet σ_{OII} ($\sigma = \sqrt{\sigma_{\text{OII}}^2 + \sigma_{\text{inst}}^2}$).

For each fitting performed, the instrumental resolution was fixed to $\sigma_{\text{inst}} = 45.4$

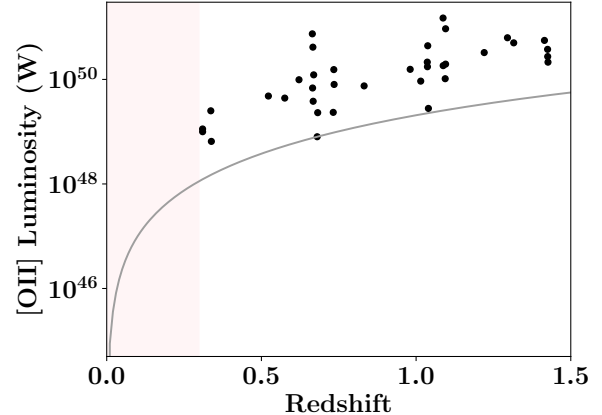


Figure 14. [OII] luminosity against redshift for 35 galaxies. Lower-limit of this sample (grey) was calculated using the object with the smallest flux. All galaxies appear above this limit and approximately follow the luminosity-redshift trend. Note that objects with $z < 0.3$ were not analysed as high-redshift galaxies were desired

km s^{-1} . This width was calculated by fitting a Gaussian curve to the sky line found at 6000 Å within a MUSE sky noise spectra. Additionally, the MUSE catalogue redshift would be used as an initial estimate for z .

Organised by V-band magnitude, it was found that only 35 galaxies contained a visible [OII] emission doublet. This corresponded to a sample limiter of ~ 25.0 mag. Subsequently, $f_{[OII]}$ calculated for these galaxies would be equivalent to the flux and [OII] luminosity of the peak. Plotting these luminosities against galaxy redshifts, as seen in Figure 14, allows for the luminosity-redshift relation to be verified for the sample. This was desired as the returned parameters from the model fitting would be used to express galaxy kinematics and it was important to understand whether they reflected physical results.

Tables II, IV provide the obtained gas velocity dispersions σ_{OII} and redshifts z for the galaxies. Quoted with each σ_{OII} value is the fractional error. The returned errors from the Python model fitting package `lmfit` (Newville et al. 2014) were not used as their origins were dubious. The methodology used to produce the fractional errors is the following: the original best fitting velocity dispersions σ_{best} and S/N between the CaH and H δ (4000 Å to 4080 Å) spectral lines were noted for the 10 brightest galaxies. The spectra for these galaxies were then perturbed 300 times with random normal noise based on the standard deviation between CaH and H δ . The new spectra would be passed to the modelling fitting routine and the [OII] doublet would be fitted for. At each perturbation step, the new velocity dispersion σ_{new} and corresponding S/N would be recorded. Then for every S/N value, the fractional error $\alpha_{\sigma_{OII}}$ could be calculated with,

$$\alpha_{\sigma_{OII}} = \frac{|\Delta\sigma|}{\sigma_{best}} = \frac{|\sigma_{best} - \sigma_{new}|}{\sigma_{best}}. \quad (3)$$

To create a quantified uncertainty value, the fractional error would be plotted against the S/N, and an a/x model applied with a as a scaling factor and x as the S/N. Figure 15a provides the plot of the fractional error model for σ_{OII} with $a = 1.88$.

Throughout this research, the fractional error method would be employed due to the undetermined nature of how model fitters

produce uncertainties. It must be noted that the z error values in the data tables are in fact the values from `lmfit`. It was decided that the fractional uncertainty method would not be directly applied for z , instead, later calculations of galaxy radial velocities which used z would estimate overall fractional errors.

In an attempt to retrieve a secondary [OII] doublet width for comparison, an alternative fitter from pPXF was used. The spectra would be passed to the Python package and a gas fitting performed where major emission lines (e.g., [OII]3727,3729; [OIII]5007; etc.) would be detected and velocity plus velocity dispersions for each line returned. However, this test proved to be unsuccessful as the routine quickly deteriorated to produce $\sigma \approx 1.0$ for a large majority of the cubes. It was suspected that this failed due to a lack of S/N for some cubes, and a failure in masking and fitting the [OII] line.

Instead, the pPXF fitting routine was used to quantify the absorption features of the galaxy spectra.

3.1.2. Absorption line modelling

With the gas kinematics of the high-redshift galaxies quantified by the [OII] emission line, a similar procedure of spectra modelling was applied to obtain the stellar kinematics from the absorption features.

The key tool within this analysis was the pPXF package. pPXF stands for penalised pixel-fitting and is used to perform parametric recovery of the line-of-sight velocity distribution of stars in a galaxy, whilst working in pixel space. The methodology was originally described by Cappellari & Emsellem (2004) and subsequently refined and upgraded in Cappellari (2017). In essence, the pPXF routine utilises a stellar spectra template library to produce spectra models. Using spectra similar to those found in Figure 8, varying numbers of templates are added together and manipulated in a χ^2 reduction routine. Velocity and velocity dispersions for the stars can then be returned from these best fitting models.

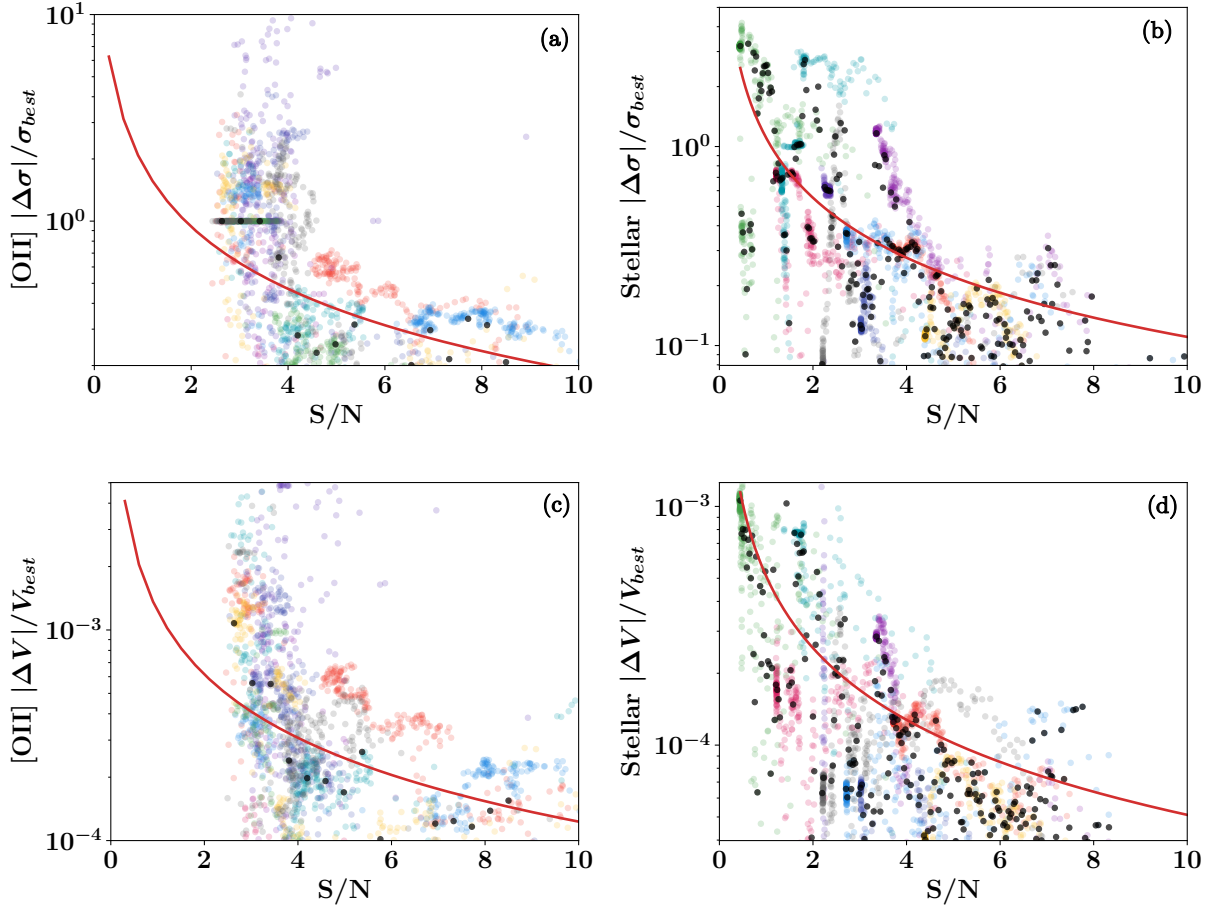


Figure 15. *Top panel:* fractional error versus signal-to-noise for stellar and [OII] gas velocity dispersions. *Bottom panel:* fractional error versus signal-to-noise for the stellar and [OII] gas velocities. *All:* the a/x models (red) provided alternative uncertainties on acquired V and σ values. The fitting routines would produce their own errors but their reliability was questioned and their methodology unknown.

The implementation of pPXF was in-part a black box routine, the data and parameters which could be passed to the procedure were: the logarithmically binned spectra, the z for the galaxy, a noise spectra, a MUSE sky noise spectra, and a spectral template set.

The noise spectra was generated by taking a region (40×34 pixel 2) in the segmentation map which appeared to be free of objects, then the standard deviation of each individual spectra pixel was calculated and then saved together as a noise spectra.

In selecting a spectral template set, it had to be ensured that one with higher spectral resolution than MUSE (~ 2.25 Å (FWHM)) was chosen. The Indo-US Lib-

rary of Coudé Feed Stellar Spectra (Valdes et al. 2004) library with spectral resolution 1.35 Å (FWHM) was selected due to the wide wavelength coverage (3460–9464 Å) and the large spectral resolution.

After the fitting routine was set up and ran, pPXF was able to return radial velocity and velocity dispersion values for the galaxy stellar component, and output the best-fitting model. Figure 16 provides an example of the optimum fitting with galaxy C1804. It appeared that pPXF was able to provide a good fitting to the spectral data as the calculated $\chi^2_\nu \approx 1.69$. However it was indicative to perform various tests and other forms of analysis to verify the reliability of the returned parameters.

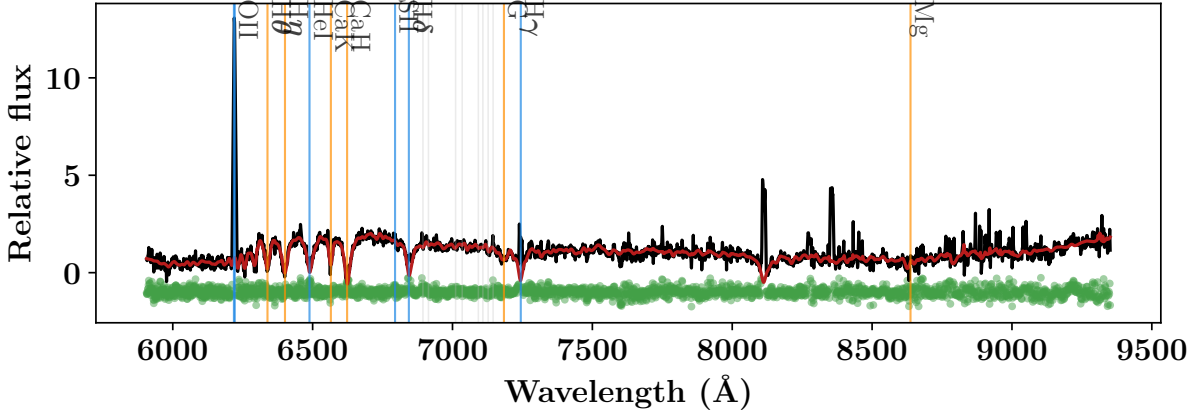


Figure 16. Spectra and best fitting pPXF model for C1804. The galaxy integrated spectra (black) would be passed to the pPXF fitting routine which would normalise the data and return a best fitting model (red) plus values for galaxy velocity and velocity dispersion. The residuals between the data and model (green) are shown in addition to some highlighted emission (blue), absorption (orange), and iron (grey) spectra features. For C1804 in particular, pPXF provided a reduced $\chi^2 \approx 1.69$ which is an indication of a good fit.

As with `lmfit`, pPXF would return values with accompanied uncertainties, and again, their origins were questioned so a fractional error model was created for the stellar velocity dispersions. Figure 15b was produced with same methodology as described in Section 3.1.1, but stellar velocity dispersions were now used σ_* and a new fitted model with $a = 1.10$.

The stellar velocity dispersions and their associated uncertainties can be found in Table II. It can be immediately seen that it was not possible to run pPXF for the entire final sample of 35 galaxies. With C109 through C1225 found in Table IV in Appendix A, these galaxies (20 objects) were found to not have enough S/N in their absorption features (hence their separation from the main report). This resulted in a smaller potential sample for the comparison of the stellar and gas kinematics in galaxies.

If the σ_* values are examined for the remaining 15 galaxies, certain results are questionable. C849, C549, and C895 are three objects in particular which stand out because of their unlikely low values of $\sigma_* \lesssim 25 \text{ km s}^{-1}$. Comparing this with the calculated value for the MUSE instrumental resolution $\sigma_{\text{inst}} = 45.4 \text{ km s}^{-1}$, it is dubious

that pPXF was able to reconstruct information which would have been lost due to instrumental convolution.

This therefore required the introduction of further sample reduction techniques to ensure that only reliable results were obtained. Employing the MUSE instrumental resolution $\sigma_{\text{inst}}/2$ (the FWHM/2), $\sigma_{\text{pPXF-limit}} \approx 22.7 \text{ km s}^{-1}$ was introduced as a lower limit in which pPXF would not be able to reconstruct velocity dispersions. Additionally, it was decided that the sample should be further restricted by the S/N of the galaxy. This was defined with the fractional error model for the stellar velocity dispersions, galaxies with $S/N \lesssim 4$ would correspond to a fractional error of $\gtrsim 27.5\%$. Beyond this percentage, the uncertainties were deemed too large and the connected result would become meaningless.

Table III provides the 15 galaxies which could be analysed by pPXF. Marked in this table are four particular galaxies which were considered unusable due to the enforced S/N and σ cut-offs. It can be seen that the uncertainties for these galaxies were severely underestimated due to the corresponding low σ_* value. In these scenarios it appeared that the pPXF uncertainties were better es-

Cube ID	S/N	σ_* (km s ⁻¹)
C1804	7.95	182(25)
C1578	10.4	117(12)
*C849	6.06	<u>3.8(7)</u>
C286	10.5	58(6)
C5	8.80	78(10)
C767	7.85	148(21)
C414	5.68	106(21)
*C549	4.95	<u>25(6)</u>
C175	5.60	127(25)
C1129	4.38	60(15)
C765	6.02	65(12)
*C1075	<u>3.86</u>	143(41)
C540	6.96	60(10)
*C895	<u>3.59</u>	<u>0.5(2)</u>
C554	6.85	123(20)

Table III. S/N, and stellar velocity dispersion values returned from pPXF for 15 galaxies. These were galaxies which could be analysed by pPXF, however, not all the results are valid. Cube IDs which are marked by * indicate the galaxy should be disregarded and the reason is demonstrated by the underlined S/N or σ_* values.

timates than the fractional error (e.g., C849: $\sigma_{\text{pPXF}} = 3.8(58)$ cf. $\sigma_{\text{FE}} = 3.8(7)$), however their origins are still doubtful.

As a comparison and test of the pPXF σ_* results, attempts were made to model the CaH and CaK absorption lines. Located at $3934.777 \times (1+z)$ Å and $3969.588 \times (1+z)$ Å, both of these lines are Voigt profiles and not Gaussian like the [OII] doublet. A model was created in lmfit using inbuilt model profiles,

$$\text{Linear}(c) + \text{Voigt}(A_1, \mu_1, \sigma) + \text{Voigt}(A_2, \mu_2, \sigma), \quad (4)$$

where c is a constant, A_1 and A_2 are the Voigt amplitudes, μ_1 and μ_2 are the locations of the peaks, and σ is the quadrature sum of the instrumental resolution σ_{inst} and width of the Voigt profiles σ_{Voigt} ($\sigma = \sqrt{\sigma_{\text{inst}}^2 + \sigma_{\text{Voigt}}^2}$).

It was found that with a standard fitting:

i.e., selecting out C1804, isolating the spectral region $3900 \times (1+z)$ Å to $4000 \times (1+z)$ Å, and running lmfit with the Voigt model; the produced fit (Figure 17a) appeared to match the general locations of the spectral lines, and the overall profile for CaK.

The produced velocity dispersion for this fit was $\sigma_{\text{Voigt}} = 281(18)$ km s⁻¹, where the uncertainties were obtained from lmfit. The quality of fit ($\chi^2_\nu = 0.0704$) did not warrant a fractional uncertainty model to be produced. Comparing σ_{Voigt} with σ_* for C1804, both values are clearly not within range of each other which prompted for a simpler model of just one Voigt profile and a linear component to test whether that could return similar values.

Excluding CaH, Figure 17b is the fitting with the reduced model. Whilst it looked like the general profile for CaK was still fitted for, the returned velocity dispersion $\sigma_{\text{Voigt}} = 289(31)$ km s⁻¹ was now further away from the pPXF result. Whilst further improvements could be made to the fitting: i.e., removing the baseline of the data, applying additional constraints, and producing custom Voigt models; it was deemed a wasteful use of time to pursue a replication of pPXXF which had taken several year's worth of research to create. Therefore, the values from pPXF were accepted from the results of testing the uncertainties, and the work in finding the optimal stellar template library.

3.1.3. σ comparisons

The sample of 11 analysed high-redshift galaxies and their obtained velocity dispersions were naturally used to compare the stellar and gas kinematics.

Figure 18 plots the sample of galaxies from Table III. The four objects which were removed from the analysis are included to demonstrate how they compare with the other galaxies.

The first form of analysis performed on the kinematic data was quantifying how well a linear model could be fitted. Three models were tested: free gradient and free intercept, fixed gradient and free intercept, and

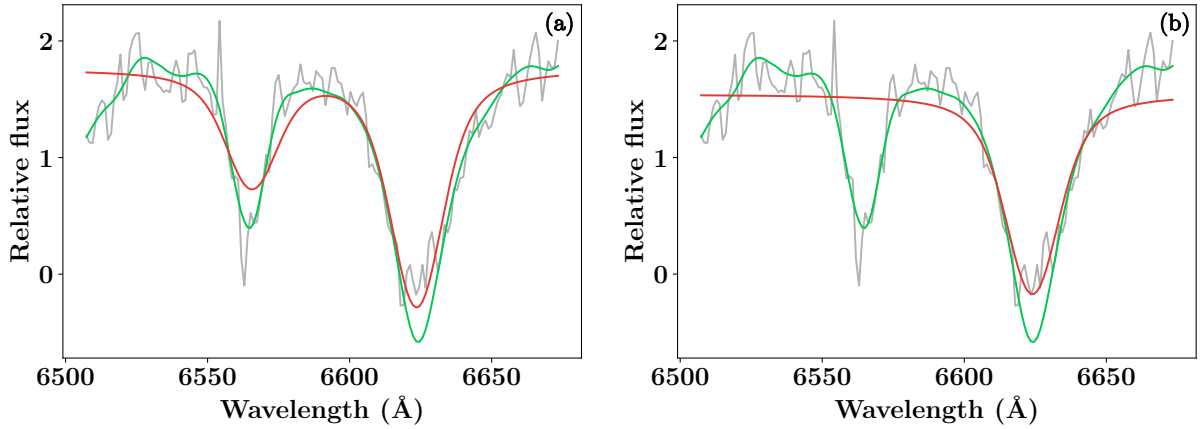


Figure 17. Attempts at Voigt modelling for CaH and CaK spectral absorption lines for C1804. (a) data (grey) was fitted with the model (red) found in Equation 4, and the best-fitting pPXF model (green) is plotted as well. (b) similar to (a), the data (grey) was plotted with the pPXF model (red), and a reduced model of just one Voigt profile (red).

free gradient and fixed intercept. When fitted to the data, the latter model appeared to be the best fit as it produced the smallest reduced χ^2 statistic of $\chi^2_\nu = 5.87$. From the presented data and within their uncertainties, the galaxies do appear to follow the linear trend. Nonetheless, the offsets still must be questioned and it should be investigated whether there is a physical reason for the galaxies to deviate.

The median ratio σ_{OII}/σ_* has a value of 1.19 (with standard deviation ~ 0.35) which could be used to indicate an offset in the scaling relations between the stars and gas, however with the calculated uncertainties this could instead imply that the scaling relations do in fact agree.

The next logical line of inquiry would be to examine whether the offsets are being driven by galaxy morphology. For the sample of galaxies within Figure 18 (including the eliminated four), they all appeared to be spiral types with features such as spiral arms, a defined disc plane, and a central nucleus bulge. So one could conclude that the general galaxy type is not prompting the materialisation of the offset.

Figure 19 provides a comparative plot of galaxy stellar and gas kinematics produced by Ho (2009), where a sample of 345

nearby galaxies ($z \lesssim 0.5$) were taken from the Palomar spectroscopic survey (Ho et al. 1995, 1997). One of the main differences in their work is that they quantified the gas kinematics through the [NII] $\lambda 6583$ emission line due to the spectral range of the double spectrograph on the Hale telescope (~ 4230 – 5110 Å and ~ 6210 – 6860 Å). Through splitting their galaxy sample into the various Hubble types (ellipticals, spirals, and lenticulars), they concluded that the correlation found between gas and stellar velocity dispersions for the entire sample is also replicated for the individual galaxy types. The previous suggestion of different morphological types driving variances in the kinematics is now looking more unlikely, however, at higher-redshifts the dynamics may potentially behave differently.

Another disparity between the work of Ho (2009) and the research presented here, is the model applied to their data. With a larger sample at hand they were able to recognise that a simple Gaussian was considered a suitable fit to their data. In this work, it is difficult to draw similar conclusions when the sample is limited to 11 galaxies.

Alternative comparisons can be made with the work of Cortese et al. (2014).

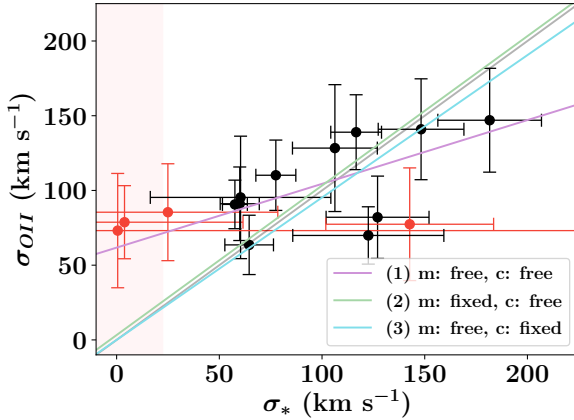


Figure 18. [OII] gas velocity dispersions (σ_{OII}) against stellar velocity dispersions (σ_*) for a sample of 11 galaxies (black). Included in this plot are four galaxies C849, C549, C1075, and C895 (red) which were removed from the sample due to low S/N or limited by the bound imposed by the FWHM/2 of MUSE (red region, $\sigma_* = 22.7 \text{ km s}^{-1}$), their original pPXF errors are used. Three linear models were fitted to the data: (1) free gradient and free intercept, $\chi^2_\nu = 6.48$; (2) fixed gradient and free intercept, $\chi^2_\nu = 6.03$; and (3) free gradient and fixed intercept, $\chi^2_\nu = 5.87$. Linear model 3 appeared to be the best fit.

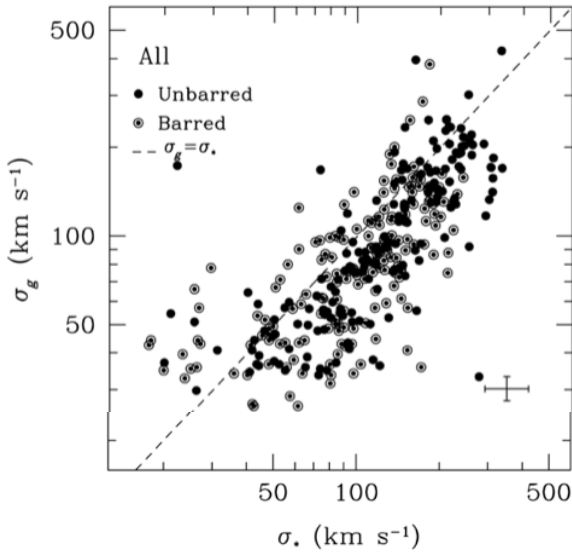


Figure 19. Gas σ_g and stellar σ_* velocity dispersion distribution for 345 galaxies of elliptical, lenticular, and spiral type from the Palomar spectroscopic survey (from Ho (2009)).

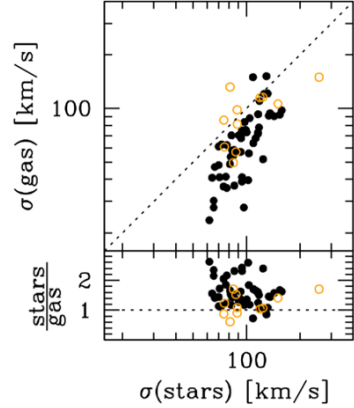


Figure 20. Gas σ_g and stellar σ_* velocity dispersion distribution for 62 galaxies from the SAMI galaxy survey (from Cortese et al. (2014)).

Shown in Figure 20 are 62 low-redshift ($0.004 < z < 0.095$) objects from the SAMI galaxy survey, their work aimed to demonstrate the possibility of a unified dynamical scaling relation for all galaxy types. What is of particular interest is their result for the kinematics between gas and stars. They derived that whilst the stars and gas scaling relations appear to be correlated, they are also offset with $\sigma(\text{gas})$ is lower than $\sigma(\text{stars})$ by a factor of 0.19 dex. Cortese et al. (2014) were able to utilise 11 emission lines ([OII] $\lambda\lambda 3726, 29$; H β ; [OIII] $\lambda\lambda 4959, 5007$; [OI] $\lambda 6300$; [NII] $\lambda\lambda 6548, 83$; H α ; and [SII] $\lambda\lambda 6716, 31$) to derive their gas velocity dispersions, something which is difficult to achieve with high-redshift data.

Comparing the results of both Ho (2009) and Cortese et al. (2014) to the research presented in this paper, it is difficult to draw certain and conclusive statements due to the limited nature of the high-redshift galaxy sample. But it does appear that the [OII] gas and stars follow a correlation which provides an indication that the [OII] emission doublet is valid for investigating the applicability of scaling relations at high-redshifts.

It was then subsequently tested whether the kinematics of different stellar populations within galaxies could be separated and

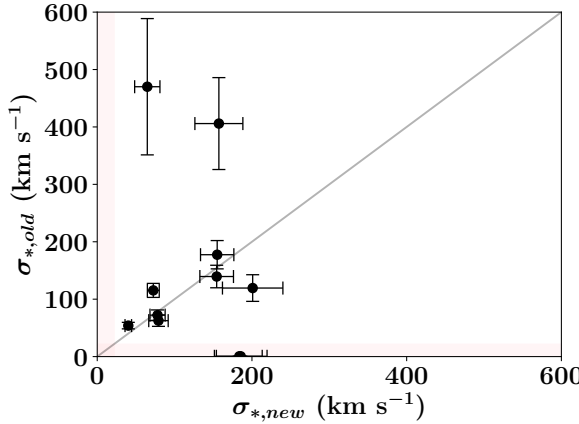


Figure 21. Velocity dispersions for old stellar types (*GK*) versus those for new (young) stellar types (*OA*). 11 galaxy spectra were isolated into overlapping regions of $3700 \times (1+z)$ Å to $4200 \times (1+z)$ Å for young stars, and $4000 \times (1+z)$ Å to $4500 \times (1+z)$ Å for old stars. If a linear trend is considered then C1129 and C175 strongly deviate from this line. This could be attributed to the difficulty in fitting for smaller wavelength regions or to problems with high noise.

demonstrated as a scaling relation. Figure 21 shows the attempt made at separating old *GK* and young *OA* stellar types. The spectra was split into two regions ($3700 \times (1+z)$ Å to $4200 \times (1+z)$ Å and $4000 \times (1+z)$ Å to $4500 \times (1+z)$ Å) and then individually passed to the pPXF routine. What is striking are the points with $\sigma_{*,old} > 300$ km s⁻¹ and $\sigma_{*,old} \approx 0$. This demonstrates clearly pPXF's inability to achieve reputable results when presented with spectra which do not contain enough information. If the dynamics of the gas and stars were seen to correlate (Figure 18), then it would be unsurprising to find that the dynamics of old and young stars correlate. Seven of the galaxies from the sample indicate this.

3.2. Galaxy velocities

Revisiting the validity of the stellar and gas results from lmfit and pPXF for the final derived sample of 11 galaxies. The galaxy radial velocities can be derived and compared.

Both routines make use of logarithmically binned spectra to derive values for

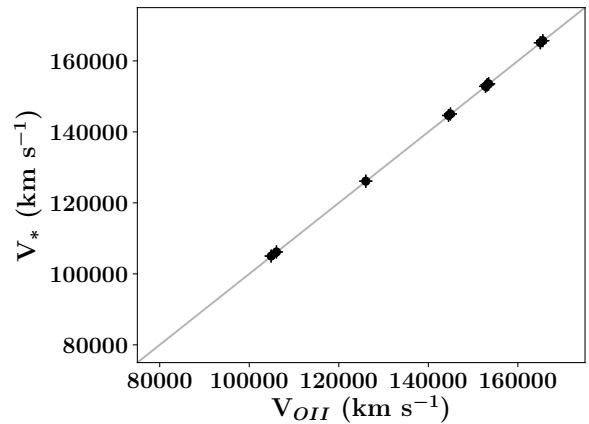


Figure 22. Stellar and [OII] gas velocities for 11 galaxies. The calculated velocities appear to be well in agreement with each other with only a 0.0757% fractional difference. Both components move at the same expected relative velocity.

galaxy redshifts, then the following equation is used to find radial velocities,

$$V = c \ln(1 + z), \quad (5)$$

where c is the speed of light, and z is the obtained galaxy redshift. Figure 22 shows that by appearance, the calculated velocities appear to be well in agreement. This is the expected result as the stars within the galaxies should trace approximately the same radial velocities as the gas.

For these velocities, fractional error models were additionally produced as seen in Figures 15c, 15d with the stellar error model using $a = 0.000510$ and [OII] with $a = 0.00123$. These uncertainty models were naturally generated as the unsurety surrounding lmfit and pPXF's generation of errors still permeated.

3.3. Voronoi tessellation

With the fitting routines validated by the velocity dispersion and velocity correlations, it was then proposed whether it was possible to subdivide the galaxy map to individually test the Tully–Fisher and Faber–Jackson scaling relations.

This process of binning the 2D galaxy map was performed with the package VorBin. As described in Cappellari & Copin

(2003) and Cappellari (2009), this routine would tessellate a galaxy map into bins based on the constraint of a minimum target S/N. Starting from the central pixel, the bins would “bloom” out and cover the entire galaxy. With the binned map, spectra could be produced for each smaller region and subsequently passed to `lmfit` and `pPXF` to produce various maps such as the radial velocity and velocity dispersions of galaxies.

To ensure that only the galaxy was binned, the segmentation maps were initially applied as a mask to the data. Then applying `VorBin` to the sample of 11 galaxies, it was found that only six objects could be tessellated. The routine would struggle to bin the 2D maps for the dimmer galaxies as they would not contain enough S/N.

The Voronoi target S/N for each galaxy was chosen so that ~ 50 bins would be produced for each galaxy. This value was selected as it was found to separate the galaxies into enough discernible individual regions. Later S/N masking would increase the difficulty in analysing the scaling relations at high-redshift.

3.3.1. Tully–Fisher

To test the Tully–Fisher relation, the end objective was to generate galaxy rotation curves and achieving this required galaxy velocity maps.

The first step was to mask the Voronoi map and remove bins with $S/N < 4$, this limit was imposed in the previous galaxy sample reduction and the reasoning is still valid here. Below this value there would not be enough information to reconstruct the galaxy kinematics. The reduced data array would then be passed to the [OII] and stellar routines and subsequent velocity maps produced from their results. The radial velocities for the central Voronoi bin was taken away from each map to produce rotational velocities.

Before the curves could be produced, the major kinematic axis of the galaxies were rotated and aligned across the horizontal. The major kinematic axis would not necessarily align with the major morphological axis

so discretion was used to rotate the maps. This procedure was applied using a combination of the returned angle from horizontal from the previous `SExtractor` results, and in-part by manually adjusting until the axis was aligned horizontally.

Once rotated, two rotation curves were produced. The first was “1D” where a 40 pixel height slice was taken across the width of the galaxy major kinematic axis and the velocities stored for each bin in that slice. The second curve was “2D” and sought to utilise the velocities from every bin for the galaxy. This was desired in a hope to improve the profiles seen from the 1D curves. However, as not all galaxies are observed face-on, their velocities and radii had to be corrected for inclination. Using the following to correct for velocities,

$$V_{los} = V_{rot} \cos i, \quad (6)$$

where V_{los} is the line of sight velocity, V_{rot} is the corrected velocity, and i is the inclination found using the semi-major (b) and semi-minor (a) parameters from the `SExtractor` routine ($\cos i = b/a$).

The radii to each bin was corrected using,

$$R_{corr}^2 = R_{obs}^2 + R_{y,obs}^2 \tan^2 i, \quad (7)$$

with R_{corr} as the corrected radius, R_{obs} is the measured radius, $R_{y,obs}$ is the y component of the measured radius, and i is the inclination angle (Johnson 2017). Note that this equation is only valid if the maps have been rotated so that the major kinematic axis is aligned horizontally.

Figure 23 demonstrates the produced segmentation map, velocity maps, the 1D and 2D rotation curves, and the absolute differences between the 1D gas and stellar velocities. Galaxy C849 appears to have its velocity dynamics flipped, however this could either be a result of low binning or a demonstration of counterrotating gas and stars. Nevertheless, it appears that 1D rotation curves could be produced for the six galaxies, with the 2D method struggling as noise from non-galaxy bins failed to be masked.

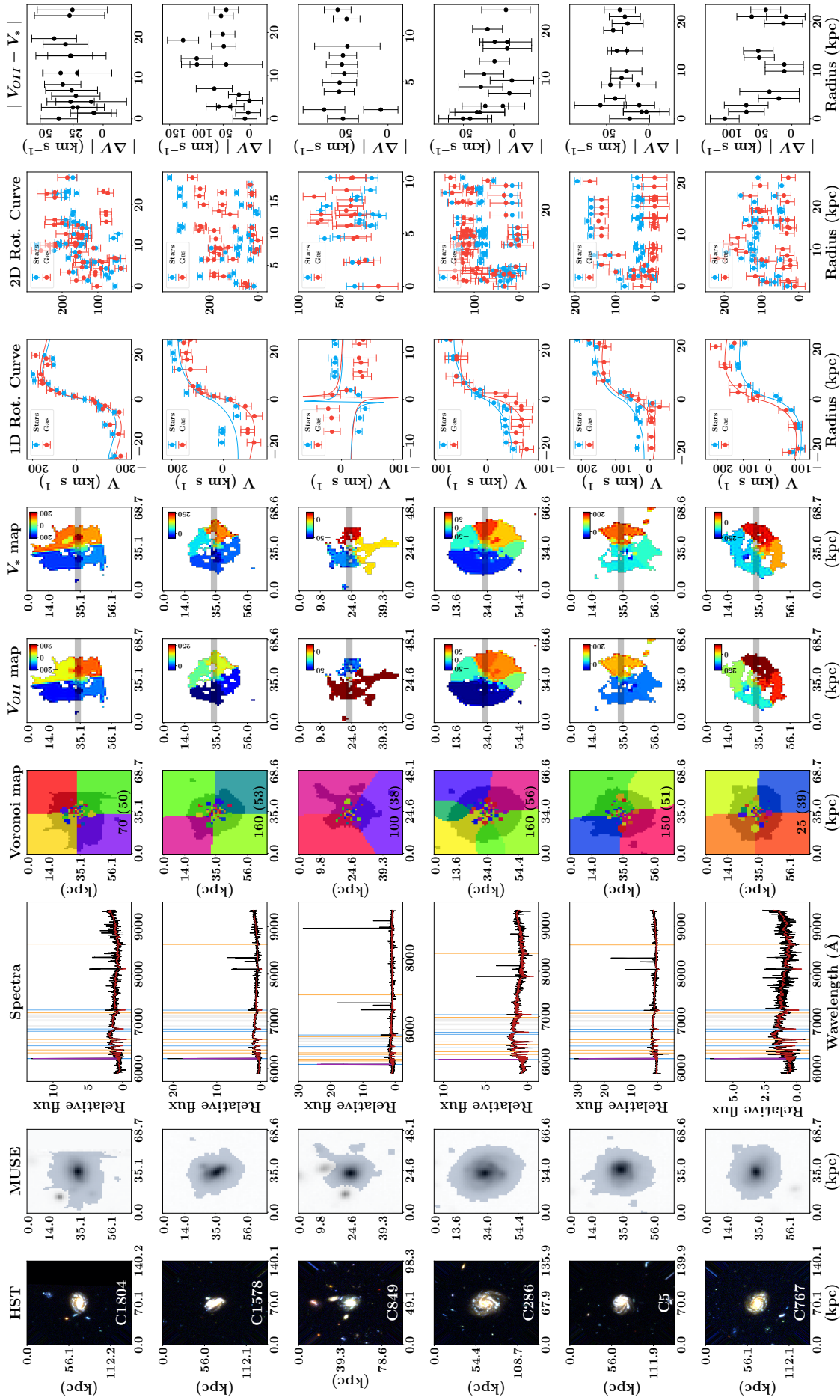


Figure 23. Voronoi tessellation analysis for six galaxies. *HST*: HST image and galaxy ID. *MUSE*: 2D MUSE optical image and segmentation area (grey). *Spectra*: galaxy data (black); pPXF model (red); and absorption (blue), emission (orange), and iron (grey) spectral lines. *Voronoi map*: Voronoi tessellated map of galaxy, segmentation area, and the target S/N with achieved bin number in brackets. V_{HII} , V_* maps: velocity fields for galaxy. *1D Rot. Curve*: rotation curve as defined by grey slice on velocity maps. *2D Rot. Curve*: rotation curves from galaxy inclination-corrected map. $|V_{\text{HII}} - V_*|$: stellar and gas velocity difference versus galaxy radius with data from 1D rotation curves.

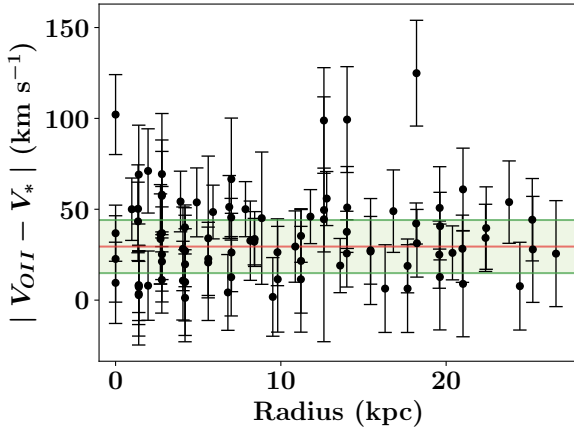


Figure 24. The absolute differences between the rotation velocities for [OII] gas and stellar for six galaxies as a function of galaxy radius. The median 29.5 km s^{-1} is marked (red) along with the area equalling 1σ (green). There appears to be a systematic offset between both galaxy components.

The absolute offsets between the [OII] gas and stellar rotation velocities were collated for the six galaxies to produce Figure 24. This plot suggests that there is a systematic offset between the gas and stars, with a median value of 29.5 km s^{-1} and a standard deviation of 14.6 km s^{-1} . This could be argued to propose that at high-redshifts of $0.3 < z < 1.6$, the gas dynamics are driven by an unknown mechanism to higher rotational velocities, or vice versa with the stellar dynamics.

In local galaxies the gas and stellar rotation curves appear to trace each other with minimal spread (Pizzella et al. 2004). An alternative possibility could be drawn to suggest that the gas and stellar dynamics do in fact agree with each other, and that there is just a computational systematic in the spectra modelling which is driving the difference. Therefore the Tully–Fisher relation could still be valid at these redshifts.

3.3.2. Faber–Jackson

The testing of the Faber–Jackson relation for high-redshift galaxies begins with applying a higher S/N mask to the Voronoi map. Instead of removing bins with $S/N < 4$, a new boundary of $S/N < 7$ was chosen. This

was applied as the spectra for bins with low S/N would struggle to recreate the profile widths, whereas this was not a considerable issue with producing radial velocities from redshifts.

In applying such a high S/N limit, this resulted in difficulty when attempting to reconstruct the velocity dispersion σ kinematics for individual galaxies. The σ maps created would not reflect the entire galaxy as large numbers of bins were masked. Subsequently, the 1D and 2D σ curves would just appear to contain noise and yield no useful results.

Figure 25 in Appendix B shows the attempt made to produce a complementary plot to Figure 23.

3.4. Limitations and future studies

What this highlights is one of the struggles faced throughout this work, low S/N in data. A large number of galaxy objects extracted from the MUSE HUDF cube were removed because of limitations in their spectra (e.g., [OII] doublet or absorption lines too dim). This issue is difficult to overcome in a variety of ways. Firstly there are limited improvements which could be made to the data itself as it has been preprocessed. Instead, the computational modelling of the spectral features could be studied to a greater extent.

In this research in particular, there was a large uncertainty surrounding how the `lmfit` and `pPXF` fitting routines function. This subsequently led to the production of fractional error models to quantify the physical limits of the packages. Future studies could work on understanding how the modelling routines function and whether custom comparative procedures could be created (e.g., successfully fitting Voigt profiles for absorption lines), thus improving the reliability of the obtained scaling relation results.

4. Conclusions

In conclusion, this project endeavoured to understand whether locally-derived scaling relations are applicable for high-redshift

galaxies. The data for the HST and MUSE HUDFs was chosen as it would provide an ideal sample of objects for those redshifts. Individual galaxies were identified from the field using **SExtractor**, and spectra data cubes extracted. The [OII] gas and stellar kinematics of the galaxies were obtained as velocity dispersions and radial velocity values from spectra modelling with **lmfit** and **pPXF** packages. Various sample reduction methods were applied such as ignoring galaxies without an [OII] emission doublet. With a reduced sample of 35 galaxies, further analysis of the S/N and absorption features would reduce this to 11 galaxies. The [OII] gas and stars in galaxies were found to correlate in the scaling relations for velocity dispersions, and radial velocities. Additionally, later testing of the Tully–Fisher and Faber–Jackson relations would highlight the issues with low galaxy S/N and spectra modelling.

Acknowledgments

The author would like to thank Dr. M. Swinbank and Dr. A. Tiley for their continual help and support throughout the project period.

The Starlink software Currie et al. (2014) is currently supported by the East Asian Observatory. This research made use of Astropy, a community-developed core Python package for Astronomy (Astropy Collaboration et al. 2013, Price-Whelan et al. 2018).

References

- Anderson J., Bedin L. R., 2010, *PASP*, **122**, 1035
- Arribas S., Koekemoer A., Whitmore B., eds, 2003, The 2002 HST Calibration Workshop : Hubble after the Installation of the ACS and the NICMOS Cooling System
- Astronomie au collège PERCERET 2012, HUBBLE TUNING FORK DIAGRAM, <http://col21-perceret.ac-dijon.fr/col-astro/spip.php?article9>
- Astropy Collaboration et al., 2013, *A&A*, **558**, A33
- Audouze J., Tinsley B. M., 1976, *ARA&A*, **14**, 43
- Baade W., 1944, *ApJ*, **100**, 137
- Bacon R., Accardo M., Adjali L., Anwand H., et al., 2010, in Ground-based and Airborne Instrumentation for Astronomy III. p. 773508, doi:10.1117/12.856027
- Bacon R., et al., 2017, *A&A*, **608**, A1
- Becker R. H., Fan X., White R. L., Strauss M. A., et al., 2001, *AJ*, **122**, 2850
- Beckwith S. V. W., Stiavelli M., Koekemoer A. M., Caldwell J. A. R., et al., 2006, *AJ*, **132**, 1729
- Bertin E., Arnouts S., 1996, *A&AS*, **117**, 393
- Blakeslee J. P., et al., 2003, in Payne H. E., Jedrzejewski R. I., Hook R. N., eds, Astronomical Society of the Pacific Conference Series Vol. 295, Astronomical Data Analysis Software and Systems XII. p. 257 ([arXiv:astro-ph/0212362](https://arxiv.org/abs/astro-ph/0212362))
- Bond H. E., 1981, *ApJ*, **248**, 606
- Cannon A. J., Pickering E. C., 1916, Annals of Harvard College Observatory, **76**, 19
- Cappellari M., 2009, arXiv e-prints, p. arXiv:0912.1303
- Cappellari M., 2017, *MNRAS*, **466**, 798
- Cappellari M., Copin Y., 2003, *MNRAS*, **342**, 345
- Cappellari M., Emsellem E., 2004, *PASP*, **116**, 138
- Cassata P., Cimatti A., Franceschini A., Daddi E., et al., 2005, *MNRAS*, **357**, 903
- Chabrier G., 2003, *PASP*, **115**, 763
- Charity M., 2016, What color are the stars? - some pixel RGB values, <http://www.vendian.org/mncharity/dir3/starcolor/>
- Cortese L., et al., 2014, *ApJ*, **795**, L37
- Crain R. A., Schaye J., Bower R. G., Furlong M., et al., 2015, *MNRAS*, **450**, 1937
- Currie M. J., Berry D. S., Jenness T., Gibb A. G., Bell G. S., Draper P. W., 2014, in Manset N., Forshay P., eds, Astronomical Society of the Pacific Conference Series Vol. 485, Astronomical Data Analysis Software and Systems XXIII. p. 391
- Dalcanton J. J., Spergel D. N., Summers F. J., 1997, *ApJ*, **482**, 659
- Driver S. P., Fernández-Soto A., Couch W. J., Odewahl S. C., et al., 1998, *ApJ*, **496**, L93
- Faber S. M., Jackson R. E., 1976, *ApJ*, **204**, 668
- Fall S. M., 1983, Internal Kinematics and Dynamics of Galaxies. Springer, pp 391–399
- Fan X., Narayanan V. K., Strauss M. A., White R. L., et al., 2002, *AJ*, **123**, 1247
- Fish R. A., 1964, *ApJ*, **139**, 284
- Fritz A., Böhm A., Ziegler B. L., 2009, *MNRAS*, **393**, 1467

- Fruchter A. S., Hook R. N., 2002, *PASP*, **114**, 144
- Giavalisco M., Ferguson H. C., Koekemoer A. M., Dickinson M., et al., 2004, *ApJ*, **600**, L93
- Grogin N. A., Lim P. L., Maybhate A., Hook R. N., Loose M., 2010, in Hubble after SM4. Preparing JWST. p. 54
- Ho L. C., 2009, *ApJ*, **699**, 638
- Ho L. C., Filippenko A. V., Sargent W. L., 1995, *ApJS*, **98**, 477
- Ho L. C., Filippenko A. V., Sargent W. L. W., 1997, *ApJS*, **112**, 315
- Hubble E. P., 1926, *ApJ*, **64**
- Illingworth G. D., et al., 2013, *ApJS*, **209**, 6
- Inami H., et al., 2017, *A&A*, **608**, A2
- Johnson H. L., 2017, PhD thesis, Durham University
- Katz N., 1992, *ApJ*, **391**, 502
- Lilly S. J., Tresse L., Hammer F., Crampton D., Le Fevre O., 1995, *ApJ*, **455**, 108
- Madau P., Dickinson M., 2014, *ARA&A*, **52**, 415
- Madau P., Ferguson H. C., Dickinson M. E., Giavalisco M., et al., 1996, *MNRAS*, **283**, 1388
- Madau P., Pozzetti L., Dickinson M., 1998, *ApJ*, **498**, 106
- McKee C. F., Ostriker E. C., 2007, *ARA&A*, **45**, 565
- Miller G. E., Scalo J. M., 1979, *ApJS*, **41**, 513
- Mo H. J., Mao S., White S. D. M., 1998, *MNRAS*, **295**, 319
- Moriya T. J., Wong K. C., Koyama Y., Tanaka M., Oguri M., Hilbert S., Nomoto K., 2019, arXiv e-prints, -
- Navarro J. F., Frenk C. S., White S. D. M., 1996, *ApJ*, **462**, 563
- Newville M., Stensitzki T., Allen D. B., Ingargiola A., 2014, LMFIT: Non-Linear Least-Square Minimization and Curve-Fitting for Python, doi:10.5281/zenodo.11813, <https://doi.org/10.5281/zenodo.11813>
- Payne C. H., 1925, PhD thesis, Radcliffe College
- Peebles P. J. E., 1969, *ApJ*, **155**, 393
- Pizzella A., Corsini E. M., Vega Beltrán J. C., Bertola F., 2004, *A&A*, **424**, 447
- Poveda A., 1958, Boletin de los Observatorios Tonantzintla y Tacubaya, **2**, 8
- Price-Whelan A. M., et al., 2018, *AJ*, **156**, 123
- Rafelski M., et al., 2015, *AJ*, **150**, 31
- Reyes R., Mandelbaum R., Gunn J. E., Pizagno J., Lackner C. N., 2011, *MNRAS*, **417**, 2347
- Romanowsky A. J., Fall S. M., 2012, *ApJS*, **203**, 17
- Salpeter E. E., 1955, *ApJ*, **121**, 161
- Sandage A., 1961, The Hubble Atlas of Galaxies. Carnegie Institution of Washington
- Sandage A., 1975, Classification and Stellar Content of Galaxies Obtained from Direct Photography. the University of Chicago Press
- Sandage A., Bedke J., 1994, The Carnegie Atlas of Galaxies. Volumes I, II.. Carnegie Institution of Washington
- Sandage A., Freeman K. C., Stokes N. R., 1970, *ApJ*, **160**, 831
- Santos N. C., Israelian G., Mayor M., 2004, *A&A*, **415**, 1153
- Schaye J., Crain R. A., Bower R. G., Furlong M., et al., 2015, *MNRAS*, **446**, 521
- Schechter P., 1976, *ApJ*, **203**, 297
- Schmidt M., 1959, *ApJ*, **129**, 243
- Slipher V. M., 1913, Lowell Observatory Bulletin, **2**, 56
- Slipher V. M., 1914, Lowell Observatory Bulletin, **2**, 66
- Somerville R. S., Davé R., 2015, *ARA&A*, **53**, 51
- Soto K. T., Lilly S. J., Bacon R., Richard J., Conseil S., 2016, *MNRAS*, **458**, 3210
- Suchkov A. A., Grogin N. A., Sirianni M., Cheng E., Waczynski A., Loose M., 2010, in Hubble after SM4. Preparing JWST. p. 55
- Taylor M. B., 2005, in Shopbell P., Britton M., Ebert R., eds, Astronomical Society of the Pacific Conference Series Vol. 347, Astronomical Data Analysis Software and Systems XIV. p. 29
- Tully R. B., Fisher J. R., 1977, *A&A*, **500**, 105
- Valdes F., Gupta R., Rose J. A., Singh H. P., Bell D. J., 2004, *ApJS*, **152**, 251
- Vega Beltrán J. C., Pizzella A., Corsini E. M., Funes J. G., et al., 2001, *A&A*, **374**, 394
- Walter F., et al., 2016, *ApJ*, **833**, 67
- White S. D. M., Rees M. J., 1978, *MNRAS*, **183**, 341
- Williams R. E., Blacker B., Dickinson M., Dixon W. V. D., et al., 1996, *AJ*, **112**, 1335
- Zwicky F., 1933, Helvetica Physica Acta, **6**, 110
- de Vaucouleurs G., 1959, Handbuch der Physik, **53**, 275
- van Dokkum P. G., Conroy C., 2012, *ApJ*, **760**, 70

Appendices

A. Remaining galaxies from sample

The remaining nine objects from the final reduced sample of 35 galaxies are presented in Table IV. These objects are part of 20 which could not be analysed due to lack of S/N in the absorption features. The model fitting routine pPXF would only successfully function with spectra containing discernible spectral lines.

It was deemed unnecessary to show the entire sample of 35 galaxies within the main body of the text as a large part of which were not used in the analysis for testing the scaling relations.

B. Voronoi Faber–Jackson plot

Voronoi analysis allowed for the binning of the galaxy maps. With this, the Tully–Fisher relation was successfully tested for galaxy radial velocities, however, it was not possible to test the Faber–Jackson relation as there was not enough remaining bins after the S/N mask was applied to the velocity dispersion maps. Figure 25 shows the attempt made to produce a complimentary set of results to the Tully–Fisher work found in Figure 23.

It was decided that Figure 25 would not be included within the main body of the paper as the produced results for each galaxy is generally too noisy to draw conclusions. It was more demonstrative to show examples of the velocity dispersion maps for a single cube, C1804, and not for all of the six successfully Voronoi tessellated galaxies.

Cube ID	RAF ID	RA (deg)	Dec. (deg)	F606W mag.	z	V_* (km s $^{-1}$)	σ_* (km s $^{-1}$)	V_{OII} (km s $^{-1}$)	σ_{OII} (km s $^{-1}$)
C1411	20647	53.16431016	-27.81082586	24.465(4)	0.73503(6)	-	-	165194(51)	113(53)
C943	6028	53.16620903	-27.7939202	24.427(7)	1.036159(9)	-	-	213172(66)	62(29)
C543	22939	53.18402132	-27.79150708	24.956(5)	1.22018(3)	-	-	239111(89)	60(34)
C1423	20544	53.16311572	-27.81360388	24.459(3)	1.42504(2)	-	-	265571(124)	67(48)
C627	8908	53.15398319	-27.77098973	24.666(8)	0.83200(4)	-	-	181496(54)	84(38)
C400	8559	53.15986702	-27.76684123	24.615(7)	1.03670(3)	-	-	213251(73)	79(41)
C1225	1742	53.16803964	-27.80741481	24.014(4)	0.30996(3)	-	-	80944(25)	59(28)

Table IV. Remaining nine objects from the 20 non-analysed galaxies which were not shown in Table II. Columns show the working cube ID, the ID from the UVUDF Catalogs (Rafelski et al. 2015) (RAF ID), the object right ascension (RA) and declination (Dec.), the magnitude of the object in the HST F606W filter, and the calculated galaxy redshift (z). Total sample contained 35 objects, 15 of which had high enough signal-to-noise in their spectra for the gas and stellar components to be analysed.

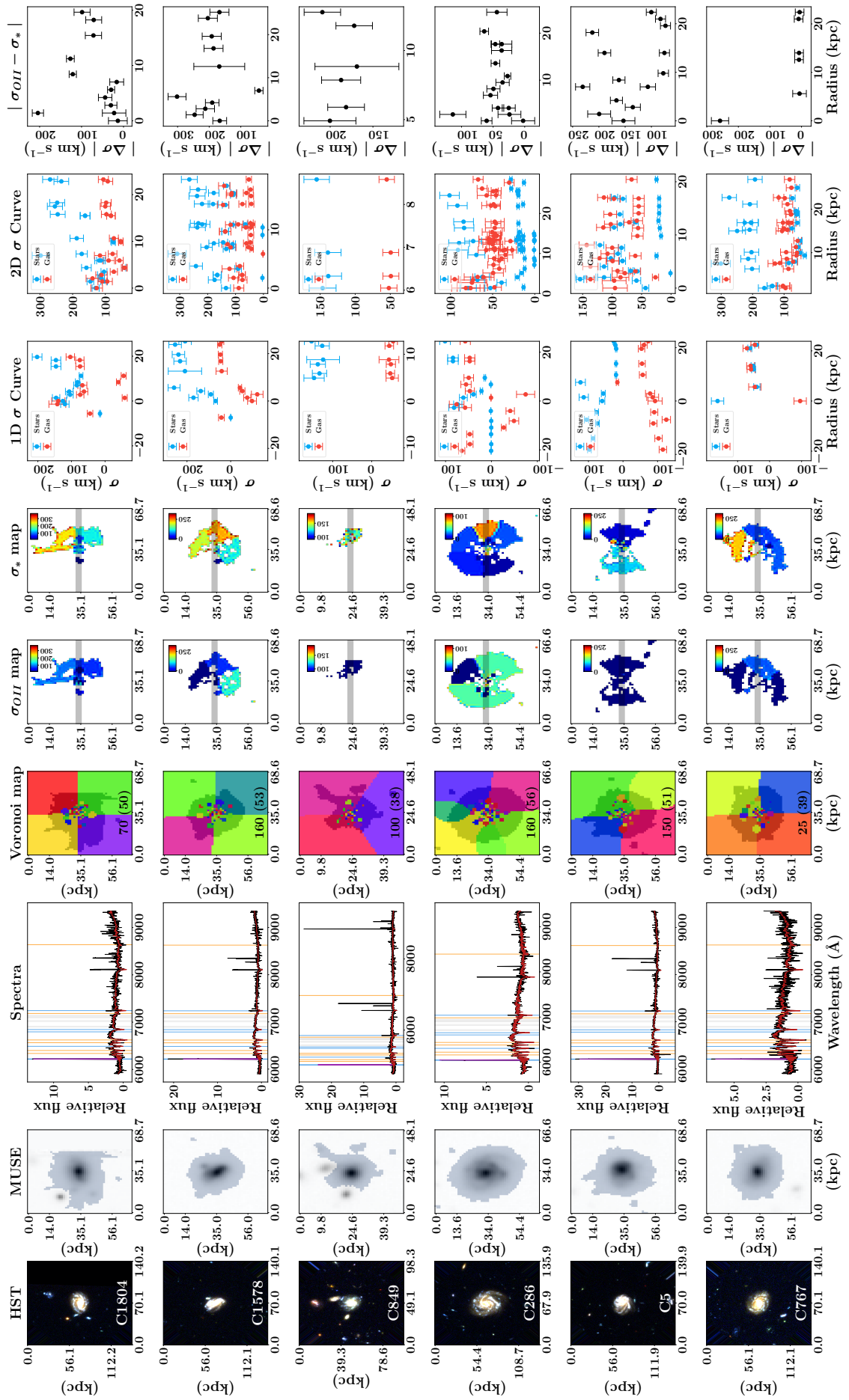


Figure 25. Voronoi tessellation analysis for six galaxies. *HST*: HST colour image and galaxy cube ID. *MUSE*: collapsed optical image from MUSE spectroscopic data and segmentation map (grey). *Spectra*: galaxy data (black); pPXF model (red); and emission (blue), absorption (orange), and iron (grey) spectral lines. *Voronoi map*: Voronoi tessellated MUSE map and segmentation area. σ_{OII} , V_* maps: velocity fields for galaxy. *1D Rot. Curve*: rotation curve as defined by grey strips on velocity maps. *2D Rot. Curve*: rotation curves from galaxy inclined-corrected map. $|\sigma_{OII} - \sigma_*|$: stellar and gas velocity difference versus galaxy radius with data from 1D rotation curves.